CARDIFF UNIVERSITY
PRIFYSGOL CAERDYDD

ORCA – Online Research @ Cardiff

This is an Open Access document downloaded from ORCA, Cardiff University's institutional repository:https://orca.cardiff.ac.uk/id/eprint/112765/

This is the author's version of a work that was submitted to / accepted for publication.

Citation for final published version:

Rugel, M., Beuther, H., Bihr, S., Ott, J., Brunthaler, A., Walsh, A., Glover, S., Goldsmith, P., Anderson, L., Schneider, N., Menten, K., Ragan, Sarah , Urquhart, J., Klessen, R., Soler, J., Roy, N., Kainulainen, J., Henning, T., Bigiel, F., Smith, R. and Longmore, S. 2018. OH absorption in the first quadrant of the Milky Way as seen by THOR. Astronomy and Astrophysics 618 , A159. 10.1051/0004-6361/201731872

Publishers page: http://dx.doi.org/10.1051/0004-6361/201731872

Please note:
Changes made as a result of publishing processes such as copy-editing, formatting and page numbers may not be reflected in this version. For the definitive version of this publication, please refer to the published source. You are advised to consult the publisher's version if you wish to cite this paper.

This version is being made available in accordance with publisher policies. See http://orca.cf.ac.uk/policies.html for usage policies. Copyright and moral rights for publications made available in ORCA are retained by the copyright holders.

Astronomy & Astrophysics manuscript no. paper_oh_interferometry
March 14, 2018
©ESO 2018

arXiv:1803.04794v1 [astro-ph.GA] 13 Mar 2018

OH absorption in the first quadrant of the Milky Way as seen by THOR⋆

M. R. Rugel[1], H. Beuther[1], S. Bihr[1], Y. Wang[1], J. Ott[2], A. Brunthaler[3], A. Walsh[4], S. C. O. Glover[5], P. F. Goldsmith[6], L. D. Anderson[7,8,9], N. Schneider[10], K. M. Menten[3], S. E. Ragan[11], J. S. Urquhart[12], R. S. Klessen[5,13], J. D. Soler[1], N. Roy[14], J. Kainulainen[1], T. Henning[1], F. Bigiel[5], R. J. Smith[15], and S. N. Longmore[16]

[1] Max Planck Institute for Astronomy, Königstuhl 17, 69117 Heidelberg, Germany
e-mail: rugel@mpia.de
[2] National Radio Astronomy Observatory, PO Box O, 1003 Lopezville Road, Socorro, NM 87801, USA
[3] Max Planck Institute for Radioastronomy, Auf dem Hügel 69, 53121 Bonn, Germany
[4] International Centre for Radio Astronomy Research, Curtin University, GPO Box U1987, Perth WA 6845, Australia
[5] Universität Heidelberg, Zentrum für Astronomie, Institut für Theoretische Astrophysik, Albert-Ueberle-Str. 2, 69120 Heidelberg, Germany
[6] Jet Propulsion Laboratory, California Institute of Technology, 4800 Oak Grove Drive, Pasadena, CA 91109, USA
[7] Department of Physics and Astronomy, West Virginia University, Morgantown WV 26506, USA
[8] Adjunct Astronomer at the Green Bank Observatory, P.O. Box 2, Green Bank WV 24944, USA
[9] Center for Gravitational Waves and Cosmology, West Virginia University, Chestnut Ridge Research Building, Morgantown, WV 26505, USA
[10] I. Physikalisches Institut, University of Cologne, Zülpicher Str. 77, 50937 Köln, Germany
[11] School of Physics and Astronomy, Cardiff University, Queen's Buildings, The Parade, Cardiff, CF24 3AA, UK
[12] School of Physical Sciences, University of Kent, Ingram Building, Canterbury, Kent CT2 7NH, UK
[13] Universität Heidelberg, Interdisziplinäres Zentrum für Wissenschaftliches Rechnen, INF 205, 69120 Heidelberg, Germany
[14] Department of Physics, Indian Institute of Science, Bangalore 560012, India
[15] Jodrell Bank Centre for Astrophysics, School of Physics and Astronomy, The University of Manchester, Oxford Road, Manchester, M13 9PL, UK
[16] Astrophysics Research Institute, Liverpool John Moores University, 146 Brownlow Hill, Liverpool L3 5RF, UK

Received XXX; accepted XXX

ABSTRACT

Context. The hydroxyl radical (OH) is present in the diffuse molecular and partially atomic phases of the interstellar medium (ISM), but its abundance relative to hydrogen is not clear.
Aims. We aim to evaluate the abundance of OH with respect to molecular hydrogen using OH absorption against cm-continuum sources over the first Galactic quadrant.
Methods. This OH study is part of the H I/OH/Recombination line survey of the inner Milky Way (THOR). THOR is a Karl G. Jansky Very Large Array (VLA) large program of atomic, molecular and ionized gas in the range $15^\circ \leq l \leq 67^\circ$ and $|b| \leq 1^\circ$. It is the highest-resolution unbiased OH absorption survey to date towards this region. We combine the optical depths derived from these observations with literature ^{13}CO(1-0) and H I observations to determine the OH abundance.
Results. We detect absorption in the 1665 and 1667 MHz transitions, that is, the "main" hyperfine structure lines, for continuum sources stronger than $F_{\rm cont} \geq 0.1$ Jy beam^{-1}. OH absorption is found against approximately 15% of these continuum sources with increasing fractions for stronger sources. Most of the absorption occurs in molecular clouds that are associated with Galactic H II regions. We find OH and ^{13}CO gas to have similar kinematic properties. The data indicate that the OH abundance decreases with increasing hydrogen column density. The derived OH abundance with respect to the total hydrogen nuclei column density (atomic and molecular phase) is in agreement with a constant abundance for $A_V < 10 - 20$. Towards the lowest column densities, we find sources that exhibit OH absorption but no ^{13}CO emission, indicating that OH is a well suited tracer of the low column density molecular gas. We also present spatially resolved OH absorption towards the prominent extended H II-region W43.
Conclusions. The unbiased nature of the THOR survey opens a new window onto the gas properties of the interstellar medium. The characterization of the OH abundance over a large range of hydrogen gas column densities contributes to the understanding of OH as a molecular gas tracer and provides a starting point for future investigations.

Key words. ISM: clouds – ISM: abundances – radio lines: ISM – surveys – molecular data – instrumentation: interferometers

1. Introduction

Molecular clouds are the hosts of star formation. Studying their physical and chemical properties, their formation, and their evolution, is crucial for understanding key characteristics of the Milky Way Galaxy, e.g., the mass of stars that can be formed

⋆ This project is based on observations made with the VLA telescope under the program IDs: 12A-161, 13A-128, 14B-148. The observations were conducted as part of the THOR survey (The H I, OH, Recombination line survey of the Milky Way; www.mpia.de/thor)

out of the gas reservoir in the Milky Way (e.g., McKee & Ostriker 2007; Dobbs et al. 2014; Heyer & Dame 2015; Klessen & Glover 2016). In particular, the formation of molecular clouds from diffuse atomic gas is of central concern.

Most molecular gas is in the form of molecular hydrogen, H_2, which is difficult to observe directly in the cold environments of molecular clouds. While CO is frequently used as a tracer of H_2 in the Milky Way (e.g., Miville-Deschênes et al. 2017), observational and theoretical studies suggest that a significant fraction of the molecular gas is not traced by CO (e.g., Grenier et al. 2005; Planck Collaboration et al. 2011; Pineda et al. 2013; Smith et al. 2014). Therefore, a search for alternative molecular gas tracers is necessary.

OH is a potential tracer for molecular gas in transition regions. It was first detected by Weinreb et al. (1963) and was one of the earliest molecules studied in detail in many regions of the Galactic plane (e.g., Goss 1968; Turner 1979; Dawson et al. 2014), as it has easily-accessible ground state transitions at cm-wavelengths. Recent high sensitivity studies found OH emission that extends beyond the molecular cloud envelope traced by CO surveys (e.g., Allen et al. 2015; Xu et al. 2016, using the GBT with 7.′6 and the Arecibo telescope with 3′ resolution, respectively). A detailed comparison of the "CO-dark" gas fraction and OH across a molecular cloud boundary in Taurus found OH to be present in "CO-dark' regions with $A_V < 1.5$ mag (Xu et al. 2016). Complementary studies show that OH is present in "partially atomic, partially molecular", warm ($\sim$ 100 K) H I halos (Wannier et al. 1993), and show that its column density increases with increasing $N_{\rm H\,I}$ for $N_{\rm H\,I} < 1.0\times10^{21}$ cm^{-2} (Tang et al. 2017). Additionally, OH has also been found to be correlated with visual extinction in diffuse clouds (Crutcher 1979, observed at 22′ resolution with the 37m telescope of the Vermilion River Observatory). These results strongly suggest its presence in transition regions between atomic and molecular gas.

The OH abundance towards higher extinction regions is on the other hand of interest for the determination of magnetic field strengths from Zeeman splitting of OH absorption lines. To understand the gas densities at which OH traces the magnetic fields, precise knowledge of the OH abundance at different densities is indispensable. In particular, the behavior of the OH abundance in regions of higher density is not yet well understood, neither theoretically nor observationally (e.g., Heiles et al. 1993).

There are three different types of chemical reactions in molecular clouds that can influence the abundance of OH (e.g., van Dishoeck et al. 2013): Gas phase ion-neutral chemistry, important in diffuse and cold environments ("diffuse" chemistry), neutral-neutral chemistry, important for warm regions (>200K), and grain surface chemistry, which depends on the strength of the radiation field and the temperature. The fractional abundance of OH is closely related to that of H_2O if diffuse chemistry or photodesorption of water from grains is dominant (Hollenbach et al. 2012). In high temperature environments, e.g., in shocks, this changes, favoring the formation of H_2O in the case of very high temperatures, unless strong ultraviolet radiation is present to photo-dissociate H_2O and thus to increase the amount of OH in the gas phase (e.g., Neufeld et al. 2002; van Dishoeck et al. 2013).

The fractional OH abundance has been found to be constant for $A_V < 7$ mag and hydrogen nuclei number densities of $n \lesssim 2500$ cm^{-3} (e.g., Crutcher 1979). Typical values for the OH abundance with respect to total hydrogen nuclei column density are $X_{\rm OH} \sim 4.0 \times 10^{-8}$ (Goss 1968; Crutcher 1979; Heiles et al. 1993), and with respect to molecular hydrogen column density $X_{\rm OH} \sim 1.0 \times 10^{-7}$ (e.g., Liszt & Lucas 2002). Other studies exist, however, which also found higher values for the OH abundance, i.e. of a few $\times10^{-7}$ in molecular cloud boundaries, with a decreasing trend towards $X_{\rm OH} \sim 1.5 \times 10^{-7}$ at visual extinctions $A_V \geq 2.5$mag (Xu et al. 2016). Once molecular cloud regions fall into the line-of-sight where UV radiation is attenuated, the OH abundance is no longer expected to be constant (Heiles et al. 1993, and references therein). Models predict the depletion of oxygen bearing species from the gas phase in the absence of photodesorption of water ice, which occurs at $A_V \sim 6$ mag, depending on the strength of the radiation field (Hollenbach et al. 2012).

The transitions investigated in this paper are the Λ doubling transitions of the OH ground state, the $^2\Pi_{3/2}$; J = 3/2 state. The transitions at 1665 MHz and 1667 MHz ("main lines") are 5 and 9 times stronger than the satellite transitions at 1612 MHz and 1720 MHz ("satellite lines"; e.g., Elitzur 1992). While the satellite lines are easily anomalously excited, e.g., through ambient infrared radiation (that is, are subject to population inversion and show non-thermal, maser emission), it requires higher densities to anomalously excite the main lines, which are mostly also found to be optically thin (e.g., Goss 1968; Crutcher 1979; Heiles et al. 1993). Observations of OH transitions at 1665 MHz and 1667 MHz in absorption against strong cm-continuum sources therefore provide a possibility to determine the optical depth of the OH ground state transitions directly (e.g., Goss 1968; Stanimirović et al. 2003).

Strong maser emission from OH 1665 and 1667 MHz has also been found, predominantly towards high mass young stellar objects, but also toward evolved stars (e.g., Argon et al. 2000). They are pumped by the strong far infrared field emitted by the warm ($T \sim 150$ K) dust in their host stars' dense ($\sim 10^7$ cm^{-3}) envelopes (e.g., Cesaroni & Walmsley 1991). In the course of the THOR survey (The H I, OH, Recombination line survey of the Milky Way; Beuther et al. 2016) many such OH masers have been detected (see, e.g., Walsh et al. 2016), but are not the topic of the present paper.

The determination of OH column densities from hyperfine ground state absorption observations requires an assumption regarding the excitation temperature of the transitions. The OH excitation temperature of the main lines depends on the volume density and ionization fraction, and only weakly on the kinetic temperature (e.g., Guibert et al. 1978). The critical density ($n_{\rm crit} = A_{\rm ul}/\gamma_{\rm ul}$; $A_{\rm ul}$ is the Einstein coefficient for spontaneous emission and $\gamma_{\rm ul}$ the collisional deexcitation rate coefficient), a measure of when collisional processes dominate the deexcitation of the upper energy levels of a transition, is typically found to be of order unity ($n \sim 1$ cm^{-3}) for the OH transitions at 1665 MHz and 1667 MHz. The transitions are typically found to be subthermally excited, with excitation temperatures of $T_{\rm ex} = 5 - 10$ K (e.g., Colgan et al. 1989). The reason for this is that densities much higher than $n_{\rm crit}$ are needed for thermalization. These densities exceed those typical of boundary regions of molecular clouds ($n \leq 10^3$ cm^{-3}). Firstly, once stimulated emission and absorption of the cosmic microwave background are included, the effective critical density required for the collisional and radiative deexcitation rates to balance is $n \gtrsim 10^3$ cm^{-3} (e.g., Wannier et al. 1993). Secondly, the small energy separation of the OH lines ($E_u/k \sim 0.1$ K) makes the lines harder to thermalize for any given $T_{\rm kin}$, such that $n \gtrsim 10^3$ cm^{-3} are required to thermalize the lines even if stimulated emission and absorption are not taken into account.

Within the THOR survey, we observed the ground state OH transitions at a high angular resolution of 20″ and compared our results to those obtained from tracers of atomic and molecular gas at comparable angular resolution across the first quadrant of the Milky Way. The present paper addresses two aspects of the OH data: The detection statistics of OH main line absorption and the utility of the OH ground state transitions as molecular and atomic gas tracers based on comparisons of column densities and kinematic properties.

The paper is structured as follows: In Section 2, we present the observations and delineate the use of ancillary data. Section 3 gives the results that are discussed in Section 4. The conclusions are provided in Section 5 and the Appendix gives additional information about the OH detections.

2. Observations and data reduction

We have mapped the four OH ground state transitions in the first quadrant of the Milky Way with the Karl G. Jansky Very Large Array (VLA) in C-configuration. The observations are part of the large program THOR, with data taken over several observational periods, mapping between $l = 14.5°$ and $l = 67.25°$, $|b| \leq 1.1°$. Here we present OH observations in absorption for the entire survey region and include the OH absorption data in the pilot study of 4 square degrees around the star-forming region W43, which have already been presented in Walsh et al. (2016). As the observing strategy was discussed in Beuther et al. (2016), we will restrict the discussion of the THOR data in this paper to the OH absorption observations.

The OH satellite line transitions, located at 1.612231 and 1.720530 GHz (Schöier et al. 2005; Offer et al. 1994), were observed with two 2-MHz-wide spectral windows. The two main line transitions at 1.665402 and 1.667359 GHz were observed in one 4-MHz-wide spectral window for $l = 29.2° - 31.5°$, $l = 37.9° - 47.1°$ and $l = 51.2° - 67.0°$. The rest of the survey coverage was mapped in the 1.665-GHz transition alone, using a 2-MHz-wide spectral window. Channel widths for all transitions are 3.9 kHz ($\sim 0.7\,\mathrm{km\,s^{-1}}$) in the pilot study ($l = 29.2° - 31.5°$, $|b| \leq 1.1°$) and 7.8 kHz ($\sim 1.4\,\mathrm{km\,s^{-1}}$) for the rest of the survey. The channel width of the OH transitions was chosen to be equivalent to the simultaneously-conducted H I observations, which in turn were following the spectral resolution of the existing H I Very Large Array Galactic Plane Survey (VGPS; Stil et al. 2006) for comparability. All data have been taken at a total integration time per pointing of 5−6 min, split into 3 observations of equal time to improve the *uv*-coverage.

The data were calibrated with the CASA calibration pipeline, and the solutions were iterated after removing data of individual baselines and antennas in time ranges in which these contain artifacts. Using CASA[1], data were continuum-subtracted and gridded on a common velocity grid of $1.5\,\mathrm{km\,s^{-1}}$ resolution, and subsequently inverted and deconvolved with the CASA task `clean`. The line free channels were cleaned separately to obtain the continuum at 1666 MHz for the 1665/1667 MHz transitions. These continuum data were used for the later analysis for consistency in calibration.

The angular resolution of the data is between 12.″7 × 12.″4 and 18.″7 × 12.″5, depending on the transition and on the elevation of the source at the time of observation. We regrid all data to the Galactic coordinate system and smooth all data to a resolution of 20″ × 20″. The noise is typically about 10 mJy beam^{-1} at a velocity resolution of $1.5\,\mathrm{km\,s^{-1}}$, except for areas around strong emission sources.

The ^{13}CO(1-0) observations employed as tracer for the molecular gas are taken from GRS (Galactic Ring Survey, Jackson et al. 2006) and for two sources that lie beyond $l = 50°$ from the Exeter FCRAO CO survey (Mottram & Brunt 2010). Both datasets were taken with a single dish telescope having a 46″ FWHM beamsize. All data have been converted to main-beam temperature (T_{mb}) using a beam efficiency of $\eta = 0.48$ (Jackson et al. 2006). The H I 21 cm absorption gives column densities of the atomic gas and the data are also from THOR (Bihr et al. 2015; Beuther et al. 2016). As the H I spectral cubes (20″ × 20″ resolution) were imaged without continuum subtraction, the continuum is extracted from the line-free channels in the provided spectral cubes and used later to derive the line-to-continuum ratio. All datasets are gridded on the same coordinate system as the 1666 MHz continuum image.

A continuum catalog was extracted from the narrow band continuum maps at 1666 MHz with a spatial resolution of 20″ × 20″ with the source finding algorithm `blobcat` (Hales et al. 2012). The noise maps were created using the residual maps that have been produced during deconvolution (see also Bihr et al. 2016). To verify the completeness of the catalog, it was matched to the continuum source catalog of the THOR survey for sources with $F_{\mathrm{cont}} \geq 0.1\,\mathrm{Jy\,beam^{-1}}$, which was derived from 128-MHz-wide spectral windows and therefore has higher sensitivity (Bihr et al. 2016, Wang et al., in prep.). One continuum source, G30.854+0.151, which was not detected in the narrow-band catalog due to strong sidelobes from a nearby continuum source, was subsequently added to the detections, and the flux from the broadband continuum catalog was used for quantitative analysis in the following.

For the quantitative comparison of OH and H I absorption to ^{13}CO(1-0) emission in Section 3.2, the spatial resolution of the OH, H I and continuum datacubes is degraded to match the resolution of ^{13}CO(1-0) data at 46”. For simplicity, the deconvolved images are smoothed with a Gaussian kernel in the image plane. The relevant quantity for absorption measurements in Sect. 3.2 is the ratio of absorption line to continuum. While the baselines of the VLA in C-configuration sample angular scales of 46”, the actual scales probed depend intrinsically on the emission structure of the continuum source. Scales of 46” are only probed for continuum emission extending at least 46” in angular size. For inhomogeneous emission, patches of stronger continuum emission will have a larger contribution to the line-to-continuum ratio. With this general consideration regarding absorption measurements, smoothing the data to 46” resolution gets closest to the scales probed by ^{13}CO emission. An example of an extended OH absorption map at 20″ × 20″ resolution is provided for the star forming complex W43 in Sect. 3.4.

To minimize the introduction of systematic errors, the continuum is derived from line-free channels and thus has the same uv-coverage and calibration as the spectral line data. The median noise in the smoothed spectral line cubes is at 0.013 Jy beam^{-1}, with variations between 0.008 Jy beam^{-1} and 0.020 Jy beam^{-1} (see also gray lines in Fig. 3). An example spectrum of all transitions is shown in Fig. 1.

To address extended OH absorption in W43 (e.g., Smith et al. 1978; Motte et al. 2014), we employ the full resolution OH 1667 MHz data (20″ × 20″). It is compared to APEX observations of 870 μm dust emission from the ATLASGAL[2] survey

[1] `http://casa.nrao.edu`; version 4.2.2

[2] `http://www.mpifr-bonn.mpg.de/div/atlasgal/`

(Schuller et al. 2009; Contreras et al. 2013; Urquhart et al. 2014) and IRAM $C^{18}O$(2-1) emission from the literature (Carlhoff et al. 2013). Both datasets were smoothed to the same spatial resolution and the $C^{18}O$(2-1) emission to the same spectral resolution as the OH data.

3. Results

3.1. Detection statistics

The OH main line transitions at 1665 MHz and 1667 MHz are searched for absorption features at the locations of peaks in the continuum maps at 1666 MHz. Absorption lines which are detected at a signal-to-noise level larger than 4 are classified as detections. In total, significant OH absorption is found against 42 continuum sources (Fig. 2).

As OH absorption can occur at multiple velocities due to clouds along the line of sight, in total we find absorption in both main lines in 59 velocity components. Of these, we find 30 and 17 velocity components exclusively in the 1665 MHz and 1667 MHz OH ground state transitions, respectively, and 12 in both lines, matching in velocity. We detect a higher number of OH 1665 MHz transitions, because the 1667 MHz transition was observed only around W43, during the pilot study, and during the second part of the THOR survey (see section 2). Conversely, we sometimes find OH features in the 1667 MHz transition that have no counterparts in the 1665 MHz transition. This is expected, as the statistical weight of this transition is roughly twice as large, hence at a given sensitivity, optical depths and column densities twice as low can be probed. Examples of these are absorption at 7.0, 51.0 and 67.5 km s^{-1} towards G29.935−0.053 (Fig. 1).

The continuum sources with detections are listed in Table 1. The spectra of the detected absorption lines are displayed in Figs. D.1 - D.7.

3.1.1. Sensitivity of the survey

The weakest continuum source with OH absorption has a continuum flux density of 0.1 Jy beam^{-1}. As shown in Fig. 3, stronger continuum sources are more sensitive to lower OH column densities. Therefore, the fraction of continuum sources that exhibit OH absorption is dependent on the continuum source strength (which sets the 4σ detection threshold, $\tau_{\rm min}$): There are 291 continuum sources above a flux density of 0.1 Jy beam^{-1} at $20'' \times 20''$ ($\tau_{\rm min} \sim 0.5$), of which 42 show OH absorption lines (14.4%). Above 1.0 Jy beam^{-1} ($\tau_{\rm min} \sim 0.04$), 13 of 29 LOS have OH absorption lines (44.8%), while above 2.0 Jy beam^{-1} ($\tau_{\rm min} \sim 0.02$), 3 out of 4 LOS (75.0%; this value should be taken with caution due to small number statistics). The cumulative detection fraction therefore is an increasing function of the continuum strength.

The reason for this increase is the dependence of the sensitivity of the optical depth (τ) on the strength of the continuum source:

$$\tau = -\ln\left(\frac{F_{\rm line}}{F_{\rm cont}} + 1\right), \quad (1)$$

where $F_{\rm line}$ is the continuum subtracted OH absorption spectrum and $F_{\rm cont}$ the continuum emission. Contributions from OH emission to the observed signal are neglected, assuming the distribution of OH is smooth enough for emission to be filtered out by the interferometric observations and due to the small OH excitation temperatures in comparison to the continuum emission (see sect. 3.2.1 for a more detailed discussion). While the OH transitions are mapped at rather uniform noise, the noise in OH optical depth, and therefore its sensitivity, is inversely proportional to continuum flux.

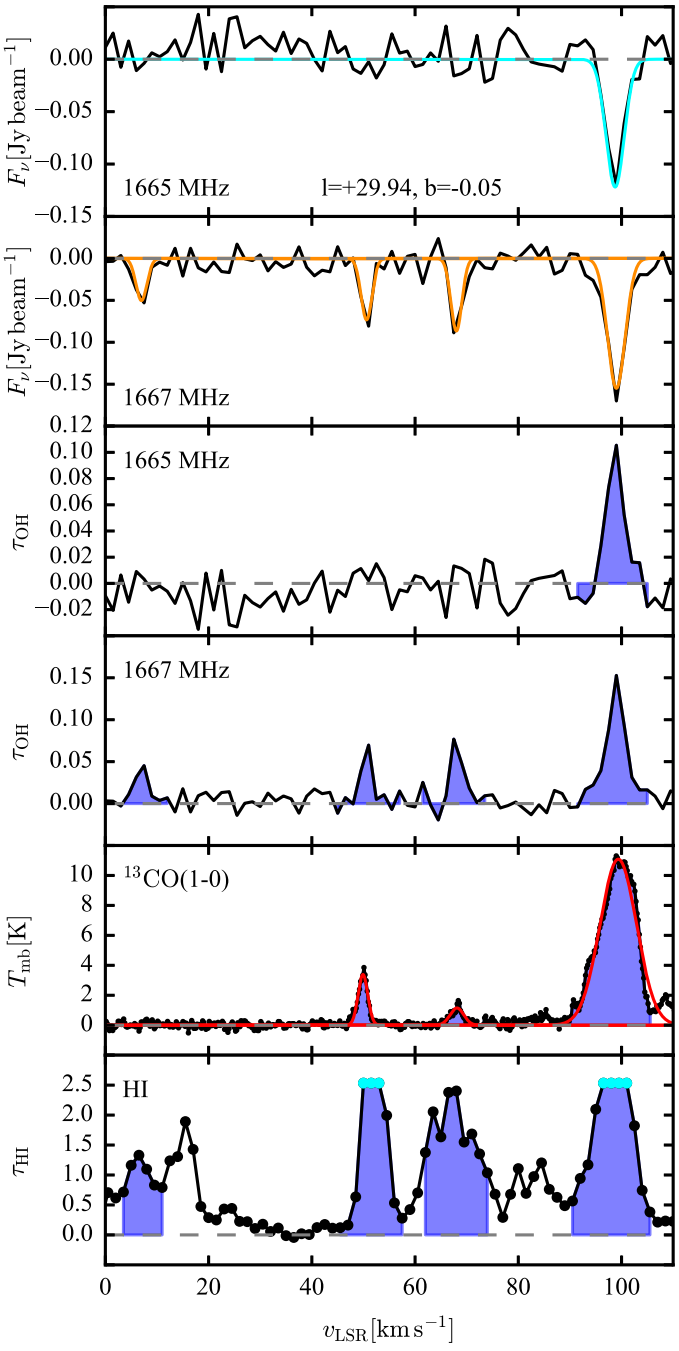

Fig. 1. Example spectra and optical depths at l=+29.935°, b=−0.053° (at 46" resolution). The topmost two panels show 1665 MHz and 1667 MHz absorption features. The fitted Gaussian profiles for the 1665 MHz line (cyan) and 1667 MHz line (orange) are overlaid. The two middle panels show the optical depth of the 1665 MHz and 1667 MHz transitions. The second panel from the bottom shows emission of ^{13}CO(1 − 0) in main-beam temperature ($T_{\rm mb}$), overlaid with a fitted Gaussian profile (red). The lowermost panel shows H I optical depth as measured from the absorption spectra. Lower limits (cyan dots) are given for saturated bins. The blue shaded area in the lower four panels denotes the area of the transitions, from which the column densities are determined.

The OH ground state main lines show maser emission against many of the strong continuum sources. Non-detection of absorp-

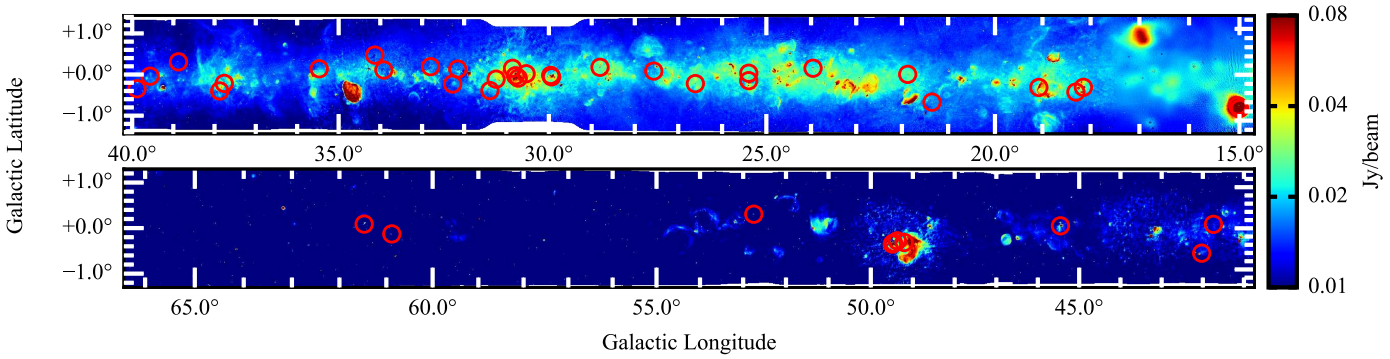

Fig. 2. Detections of OH absorption at 1665 and 1667 MHz (red circles) overplotted on continuum emission at 1.4 GHz from the combined THOR and VGPS data (Beuther et al. 2016, Wang et al., in prep.).

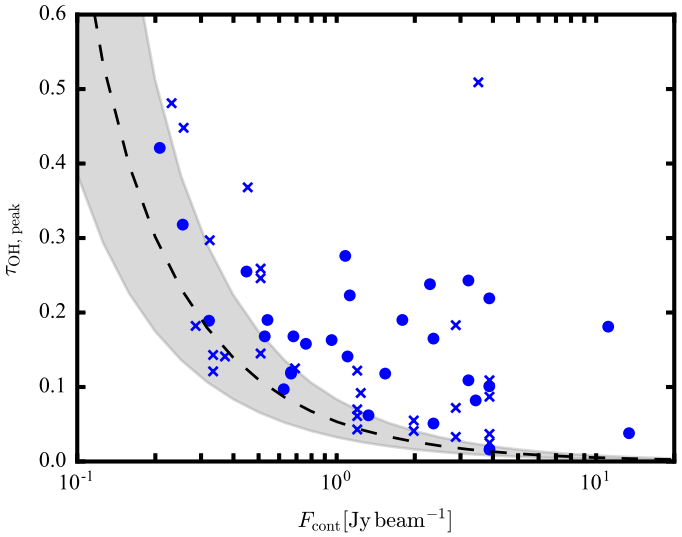

Fig. 3. Peak optical depth of the 1665-MHz transition (circles) and the 1667-MHz transition (crosses) versus continuum flux density at 46″. The sensitivity in OH optical depth is indicated by an average 4-σ detection limit (black dashed curve). Variations in the detection limit among sightlines are indicated by the gray shaded area.

tion lines is therefore not indicative of absence of OH in these lines of sight, but points to OH having different excitation conditions. Such regions typically have high dust temperatures and local densities ($T_{\rm dust} > 80$ K, $n_{\rm H_2} > 10^5$ cm^{-3}; e.g., Cesaroni & Walmsley 1991, Guibert et al. 1978, Csengeri et al. 2012, Elitzur 1992, and references therein).

Artifacts also influence some of the spectra. This can be due to increased noise caused by residual radio frequency interference (RFI), which should be minor, as the data have been closely inspected for RFI prior to imaging. Also, strong line emission of non-thermal origin can leave various traces. At the position of a maser, adjacent channels are affected by Gibbs ringing, which is a recurring pattern in velocity of emission and absorption. If the maser emission is strong, channel maps around the peak velocity of the emission can be affected by increased noise levels and sidelobes. In the case of W51 Main (e.g., Ginsburg et al. 2012; G49.488−0.380 in this work), for example, it is difficult to discern negative sidelobes from true absorption. Absorption is present in this region as it is different from the shape of the interferometry pattern. Both, however, overlap and therefore a quantitative analysis of the affected velocity channels is not possible.

3.1.2. H II region associations

In order to classify the continuum sources, we compare their location and the velocity of the detections to the emission from Radio Recombination Lines (RRLs) as reported in the WISE[3] catalog of H II-regions (Anderson et al. 2014). The spatial selection criterium is overlap with the H II-regions using their angular sizes as reported in the WISE catalog. Since typical velocity differences between H II regions and associated molecular gas are lower than 10 km s^{-1} (Anderson et al. 2009, 2014), we use this as criterium for association in velocity.

For completeness, we also search the RRL observations in THOR (Beuther et al. 2016) and catalogs of dense molecular gas tracers associated with compact and ultracompact H II regions (e.g., NH_3, HCO^+; ATLASGAL survey; Urquhart et al. 2013; Contreras et al. 2013; Urquhart et al. 2014). While not adding new sources, counterparts of many OH detections could be found also in these datasets.

To confirm the presence H II-regions, we obtain information on the spatial extent and the spectral index of the continuum sources from the THOR continuum source catalog (Bihr et al. 2016; Wang et al. in prep.). As H II regions would be located in our Galaxy, they are likely to be spatially resolved within THOR. The spectral index between 1 and 2 GHz helps to distinguish between thermal (with a spectral index of $\alpha \gtrsim -0.1$) and non-thermal emission sources (with a spectral index of $\alpha \sim -1$). Most of the continuum sources with RRL counterparts show thermal emission and are spatially resolved.

In total, 47 OH absorption components have its origin in molecular gas that is associated with H II regions in position and velocity, which represent 80% of all detections (see discussion in Sect. 4.1). We find that 38 out of 42 of the cm-continuum sources, against which the detections occur, show evidence of being H II regions. Three of the four other continuum sources are likely to be of extragalactic origin, as they are spatially unresolved and show non-thermal emission.

Twelve velocity components in the 1665 MHz and 1667 MHz transitions, of which 4 are detected in both, originate from clouds that are not associated with H II regions. Neither RRL emission in the WISE catalog, nor dense molecular gas tracers are reported at the same $v_{\rm LSR}$. The peak optical depth is lower than seen for sources associated with H II regions. Accordingly, these absorption features are likely to originate from foreground, potentially diffuse clouds.

[3] astro.phys.wvu.edu/wise/

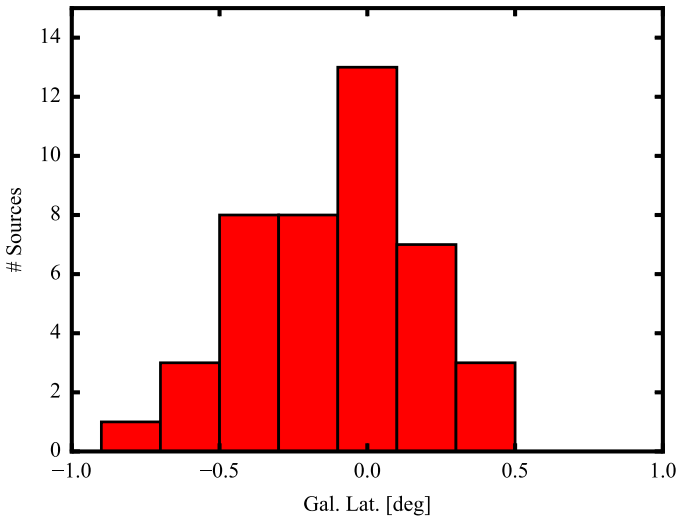

Fig. 4. Number of continuum sources with OH absorption detections versus Galactic latitude.

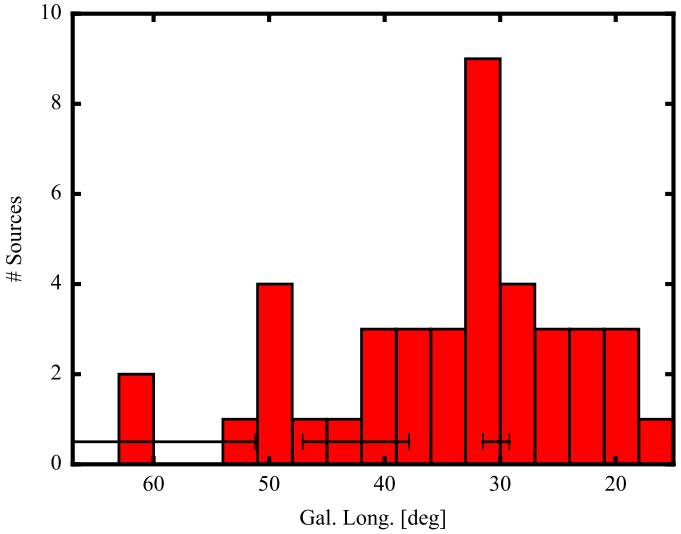

Fig. 5. Number of continuum sources with OH absorption detections versus Galactic longitude. The 1665 MHz transition was observed over the entire region of the survey. The coverage of the 1667 MHz transition is indicated by the black bars.

3.1.3. Distribution of sources in the Galactic plane

The distribution of OH absorption detections is strongly concentrated towards the Galactic midplane (Figs. 5 and 4), while relatively few detections are made at $|b| > 0.5°$. This follows the distribution of resolved Galactic continuum sources as a function of Galactic latitude (e.g., Bihr et al. 2016). Figure 4 is slightly skewed towards negative Galactic latitudes. This may be due to the sun being located above the true galactic plane, while the sun is located at b=0.0° in the Galactic coordinate system (Blaauw et al. 1960; Ragan et al. 2014). Depending on the distance of the object and the assumptions used to determine the physical location of the galactic plane, sources which lie, e.g., in the Scutum–Centaurus Arm have galactic latitudes of $b = [-0.4°, -0.1°]$ (see discussion in, e.g., Goodman et al. 2014), which agrees well with the observed extent of the source distribution towards lower Galactic latitudes.

The histogram of sources versus Galactic longitude (Fig. 5) reflects the Galactic structure, with a peak in the number of OH absorption sources at longitudes $l = 30°$ and 50°, which are the tangential points of the Scutum and Sagitarius spiral arms, respectively (e.g., Reid et al. 2014). This confirms that most of the continuum background sources, against which OH absorption is seen, are of Galactic origin, as already indicated by the large number of H II regions in our sample.

3.2. OH abundance

3.2.1. Line integrals

The OH column density is derived from the integrated optical depth in the main line transitions under the assumption that all molecules are in the four sublevels of the ground state arising from the Λ doubling and hyperfine structure (e.g., Elitzur 1992). The derived column densities are listed in Table 3.

Optical depths are computed from the line-to-continuum ratio. Contributions from large-scale emission are assumed to be filtered out by the interferometer. The emission term in the radiative transfer equation which includes the excitation temperature is therefore negligible ($T_{\rm line} = (T_{\rm ex} - T_{\rm cont})(1 - e^{-\tau})$; where $T_{\rm line}$ and $T_{\rm cont}$ can be derived in Raleigh-Jeans approximation from the continuum-subtracted line flux and the continuum flux, $F_{\rm line}$ and $F_{\rm cont}$). Even if this assumption did not hold true, at excitation temperatures of about $T_{\rm ex} = 5 - 10$ K, the approximation $T_{\rm cont} \gg T_{\rm ex}$ underestimates the optical depth for a 5-σ detection by less than $\ll$10% at 20″ resolution and for sources with $F_{\rm cont} > 0.5$ Jy beam^{-1} at 46″ resolution. For weaker sources which show detectable extended continuum emission, the underestimation would be between 6-16% after smoothing to 46″.

The integrated optical depth is determined by summation over all spectral bins of the absorption feature. The ^{13}CO(1-0) emission is integrated over the same velocity range. If a corresponding ^{13}CO(1-0) feature exists that is broader than the OH feature, the velocity range is chosen to enclose the ^{13}CO(1-0) feature (see Fig. 1). For lines that have no ^{13}CO(1-0) detection counterpart, 3-σ upper limits are given for integrated emission and all derived quantities, under the assumption of an average line width of 4.0 km s^{-1} of the detected ^{13}CO emission (Table 3).

Similarly, we derive the optical depth of H I from the line-to-continuum ratio, and give lower limits in the case of saturated absorption. A saturated channel is defined here as observed flux that is within 3-σ of the zero level. This value is then used to calculate the lower limit (see cyan circles in the lowermost panel of Fig. 1). Analogously to the discussion above on $\tau_{\rm OH}$, emission in principle also affects the H I optical depth, but is likely to be filtered out here. For this reason, we do not attempt to correct for it, but note that the integrated optical depth here always represents a lower limit.

3.2.2. OH column density

The OH column density is inferred for each main line separately, under the assumption that all OH molecules are in the ground state, $^2\Pi_{3/2}(J = 3/2)$. The OH column density is given by (e.g., Stanimirović et al. 2003)

$$\frac{N_{\rm OH}}{T_{\rm ex}} = \frac{C_0}{f} \int \tau \, dv, \qquad (2)$$

where $N_{\rm OH}$ is the total OH column density in cm^{-2}, $T_{\rm ex}$ the excitation temperature in Kelvin, $C_0 = 4.0 \times 10^{14}$ cm^{-2} K^{-1}km^{-1}s for the 1665 MHz transition and $C_0 = 2.24 \times 10^{14}$ cm^{-2} K^{-1}km^{-1}s

Table 1. Lines of sight with detections of the OH 1665/1667 MHz transitions.

Name	RA (J2000) (h m s)	Dec. (J2000) (° ′ ″)	$F_c(20'')$ $\left[\frac{\text{Jy}}{\text{beam}}\right]$	$F_c(46'')$ $\left[\frac{\text{Jy}}{\text{beam}}\right]$	Ext.	α	OH velocities $\left[\frac{\text{km}}{\text{s}}\right]$	Ass. H II	H II-region
G14.490+0.021	18 16 46.666	−16 20 33.15	0.2	0.2	1	+0.0	(23.1)	(1)	G014.489+00.020
G14.996−0.738	18 20 33.756	−16 15 22.46	1.1	3.4	1	+0.7	21.8	1	G015.035−00.677; M17; S45
G15.033−0.679	18 20 25.129	−16 11 43.00	3.4	13.4	1	+0.7	12.9	1	G015.035−00.677; M17; S45
G18.148−0.283	18 25 01.009	−13 15 30.78	0.4	1.1	1	+0.1	56.4	1	G018.144−00.286
G18.303−0.390	18 25 42.284	−13 10 18.26	0.8	1.1	1	+0.4	(27.2), 32.2, (36.2)	(1), 1, (1)	G018.305−00.391
G19.075−0.288	18 26 48.526	−12 26 28.66	0.4	0.7	1	+0.4	64.6	1	G019.066−00.281; W39
G21.347−0.629	18 32 20.815	−10 35 11.37	1.0	1.0	0	+0.0	56.1	0	
G21.874+0.007	18 31 02.524	−09 49 30.49	0.5	0.6	1	+0.3	21.8	1	G021.870+00.010
G23.956+0.150	18 34 25.303	−07 54 46.37	0.9	1.3	1	+0.6	80.0	1	G023.956+00.152
G25.396+0.033	18 37 30.623	−06 41 16.38	0.3	0.4	1	+0.4	−12.1	1	G025.396+00.034
G25.397−0.141	18 38 08.202	−06 45 58.85	1.6	2.4	1	+0.8	67.1, 94.5	1, 1	G025.383−00.177
G26.609−0.212	18 40 37.495	−05 43 19.00	0.2	0.2	1	+0.3	−33.2	1	G026.610−00.212a
G27.563+0.084	18 41 19.379	−04 44 17.57	0.1	0.1	1	+0.2	86.0	1	G027.562+00.084
G28.806+0.174	18 43 16.959	−03 35 28.97	0.3	0.7	1	+0.1	79.8, 103.5	0, 1	G028.801+00.174
G29.935−0.053	18 46 09.525	−02 41 27.54	0.5	1.2	1	+0.1	7.0, 50.6, 68.0, 98.9	0, 0, 0, 1	G029.945−00.039; G29
G29.957−0.018	18 46 04.241	−02 39 19.25	1.4	2.0	1	+0.9	8.0, 99.8	0, 1	G029.945−00.039; G29
G30.535+0.021	18 46 59.359	−02 07 26.40	0.5	0.7	1	+0.6	(43.7, 49.4), 91.6	(1, 1), 1	G030.539+00.024
G30.720−0.083*	18 47 41.713	−02 00 23.48	0.4	–	0	+1.0	93.6	1	G030.782−00.028; W43
G30.783−0.028	18 47 36.898	−01 55 30.26	1.3	3.9	1	+0.3	77.9, 81.9, 87.1	1, 1, 1	G030.782−00.028; W43
							92.1, 98.6	1, 1	
G30.854+0.151	18 47 06.546	−01 46 49.14	0.1	0.3	1	−0.1	95.4	1	G030.852+00.149a
G31.242−0.110	18 48 44.821	−01 33 14.65	0.4	0.5	1	+0.5	19.6, 79.2, 83.7	1, 0, 0	G031.239−00.108
G31.388−0.383	18 49 59.195	−01 32 56.04	1.2	1.2	0	−0.9	18.1	0	
G32.151+0.132	18 49 32.499	−00 38 05.79	0.4	0.5	1	+0.4	93.8	1	G032.160+00.130
G32.272−0.226	18 51 02.358	−00 41 24.22	0.3	0.3	1	+0.2	22.6	1	G032.272−00.226
G32.798+0.190	18 50 31.084	−00 01 56.81	1.2	1.5	1	+1.0	12.8	1	G032.960+00.276
G32.928+0.607	18 49 16.315	00 16 23.85	0.2	0.3	1	+0.4	(−33.9)	(1)	G032.928+00.607
G33.915+0.110	18 52 50.381	00 55 29.56	0.6	0.8	1	+0.5	(95.3, 101.5), 106.3	(1, 1), 1	G033.910+00.110
G34.132+0.471	18 51 57.102	01 16 58.86	0.4	0.5	1	+0.2	33.8	1	G034.133+00.471
G35.467+0.139	18 55 34.169	02 19 11.16	0.2	0.3	1	+0.6	77.0	1	G035.470+00.140
G37.764−0.215	19 01 02.118	04 12 03.76	0.4	1.1	1	+0.1	63.4	1	G037.760−00.200
G37.874−0.399	19 01 53.641	04 12 52.52	1.3	1.8	1	+0.5	61.0	1	G037.870−00.400; W47
G38.876+0.308	19 01 12.538	05 25 44.28	0.2	0.2	0	+0.8	−16.3	1	G038.875+00.308
G39.565−0.040	19 03 43.340	05 52 55.41	0.4	0.5	0	−0.9	23.2	0	
G39.883−0.346	19 05 24.156	06 01 28.52	0.2	0.3	0	+0.8	56.9	1	G039.883−00.346
G41.741+0.097	19 07 15.655	07 52 42.12	0.3	0.3	1	+0.3	14.2	1	G041.740+00.100
G42.027−0.604	19 10 18.252	07 48 32.39	0.3	0.4	1	−1.0	65.1	0	
G45.454+0.060	19 14 21.188	11 09 12.92	1.4	2.9	1	+0.4	56.0, 59.4, 64.9	1, 1, 1	G045.454+00.059; K47
G49.206−0.342	19 23 00.834	14 16 50.73	0.8	2.3	1	+0.2	65.3	1	G049.205−00.343; W51
G49.369−0.302	19 23 11.204	14 26 37.06	1.5	3.2	1	+0.5	50.9, 62.9	1, 1	G049.384−00.298; W51
G49.459−0.353	19 23 32.908	14 29 55.71	1.9	3.9	1	+1.3	62.0, 68.6	1, 1	G049.490−00.381; W51
G49.488−0.380	19 23 42.119	14 30 41.99	4.0	11.1	1	+1.3	65.9	1	G049.490−00.381; W51
G52.753+0.334	19 27 32.385	17 43 27.32	0.3	0.3	1	+0.1	12.1, 45.2	1, 0	G052.757+00.334
G60.882−0.132	19 46 20.621	24 35 17.59	0.2	0.3	1	+0.0	22.3	1	G060.883−00.133; S87
G61.475+0.092	19 46 48.189	25 12 47.06	2.1	3.5	1	+0.5	(5.9), 21.1	(0), 1	G061.477+00.094; S88

Notes. The source name is constructed from the Galactic coordinates at which the peak of the continuum emission measured at 20″ resolution occurs. The columns F_c denotes the flux density at the given coordinates for an angular resolution of 20″ and 46″. The column "Ext." denotes whether the sources is resolved (*1* for resolved, *0* for unresolved sources), and the column α is the L−band spectral index, defined as $I(\nu) \propto \nu^{\alpha}$, which are both taken from Bihr et al. (2016) and Wang et al. (in prep.). The central velocities of detected OH main line absorption are summarized in column 8 "OH velocities" (tentative, 3-σ components are listed in brackets in column 8 and 9). Association in position and velocity with an H II region is indicated with *1* in column 9. Criteria for the association are a smaller angular separation from the H II region than its radius, and a velocity difference of less than 10 km s^{-1}. The name of the H II regions are obtained from the WISE catalog of H II-regions (Anderson et al. 2014).
Footnotes: (*) Used 20″ resolution data only in order not to blend OH absorption with adjacent maser.

for the 1667 MHz transition (e.g., Goss 1968; Turner & Heiles 1971; Stanimirović et al. 2003, calculated using Einstein coefficients from Turner 1966). The filling factor f describes the solid angle fraction of the continuum source that is covered by the OH cloud. We assume that $f = 1$. The 1667 MHz transition is expected to be detected at higher signal-to-noise than the 1665 MHz transition because of its larger statistical weight, and therefore the 1667 MHz transition is used for further analysis whenever available. The calculated $\frac{N_{\rm OH}}{T_{\rm ex}}$ ratios are given in Table 3.

The excitation temperatures of the OH transitions cannot be derived independently from their optical depth, as local thermal equilibrium between the levels of the two main lines is not necessarily given, and thus the excitation temperatures of both main lines may be different (e.g., Crutcher 1979; Dawson et al. 2014). A determination of both $T_{\rm ex}$ and τ is in principle possible if addi-

Table 2. Line properties of OH 1665/1667 MHz absorption and ^{13}CO(1-0) emission.

Name	OH 1665 MHz					OH 1667 MHz					^{13}CO(1 − 0)				Ass.	Int. Range	Notes	
	v	Δv	$F_{\rm peak}$	$\tau_{\rm peak}$	$\int\tau{\rm dv}$	v	Δv	$F_{\rm peak}$	$\tau_{\rm peak}$	$\int\tau{\rm dv}$	v	Δv	$T_{\rm mb,p}$	$\int T_{\rm mb}{\rm dv}$			FWHM	Int.
	[km/s]	[km/s]	[Jy/beam]		[km/s]	[km/s]	[km/s]	[Jy/beam]		[km/s]	[km/s]	[km/s]	[K]	[K km/s]	H II	[km/s, km/s]		
G14.490+0.021	23.1	2.9	−0.06	0.34[a]	<1.35	–	–	–	–	–	–	–	–	–	(1)	[+19.4, +27.1]	2(OH)	2(OH)
G14.996−0.738	21.8	4.0	−0.28	0.08	0.37	–	–	–	–	–	–	–	–	–	1	[+16.0, +28.0]	1	1
G15.033−0.679	12.9	5.4	−0.49	0.04	0.21	–	–	–	–	–	–	–	–	–	1	[+7.0, +16.6]	1	1
G18.148−0.283	56.4	3.5	−0.22	0.22	0.81	–	–	–	–	–	55.5	3.7	6.81	32.84	1	[+51.2, +61.0]	1665	1665
G18.303−0.390	27.2	4.3	−0.04	0.03[a]	–[b]	–	–	–	–	–	–	–	–	–	(1)	–	3(OH)	3(OH)
	32.2	2.5	−0.15	0.14	0.47	–	–	–	–	–	33.0	4.1	7.69	34.90	1	[+27.0, +38.0]	4(CO)	1665
	36.2	2.5	−0.02	0.02[a]	–[b]	–	–	–	–	–	–	–	–	–	(1)	–	3(OH)	3(OH)
G19.075−0.288	64.6	7.4	−0.11	0.17	1.35	–	–	–	–	–	65.1	6.1	7.52	55.94	1	[+56.9, +75.0]	4(OH)	1665
G21.347−0.629	56.1	2.5	−0.15	0.16	0.47	–	–	–	–	–	56.2	1.8	3.43	21.95	0	[+48.0, +58.6]	1665	4(CO)
G21.874+0.007	21.8	8.8	−0.08	0.10	1.01	–	–	–	–	–	22.3	4.9	5.86	30.52	1	[+15.5, +27.0]	5(OH)	1665
G23.956+0.150	80.0	5.5	−0.08	0.06	0.38	–	–	–	–	–	79.6	3.6	9.31	38.99	1	[+74.9, +86.1]	4(CO)	1665
G25.396+0.033	−12.1	2.7	−0.10	0.25	0.80	–	–	–	–	–	–	–	–	–	1	[−15.1, −8.9]	1	1
G25.397−0.141	67.1	5.3	−0.12	0.05	0.26	–	–	–	–	–	66.5	5.7	1.75	10.12	1	[+61.4, +72.5]	4(CO)	1665
	94.5	5.8	−0.35	0.17	0.96	–	–	–	–	–	96.3	6.9	8.04	60.09	1	[+88.0,+105.0]	4(CO,OH)	1665
G26.609−0.212	−33.2	2.5	−0.07	0.42	0.77	–	–	–	–	–	–	–	–	–	1	[−37.6, −29.9]	1	1
G27.563+0.084	86.0	2.5	−0.06	0.61	1.81	–	–	–	–	–	85.8	3.2	3.30	29.90	1	[+78.0, +89.0]	5(OH)	1665
G28.806+0.174	79.8	2.5	−0.08	0.12	0.39	–	–	–	–	–	80.6	3.1	2.26	10.72	0	[+76.4, +83.0]	4(CO)	1665
	103.5	3.8	−0.07	0.12	0.38	–	–	–	–	–	104.8	5.6	6.57	41.67	1	[+98.0,+115.0]	1665	4(CO)
G29.935−0.053	–	–	–	–	<0.14	7.0	2.5	−0.05	0.04	0.11	–	–	–	<2.34	0	[+2.0, +12.0]	2(CO)	1667
	–	–	–	–	<0.15	50.6	2.5	−0.08	0.06	0.14	49.9	2.2	3.39	8.32	0	[+47.0, +53.0]	5(CO)	1667
	–	–	–	–	<0.14	68.0	2.5	−0.09	0.07	0.19	68.1	3.1	1.15	4.20	0	[+61.0, +74.0]	5(CO)	1667
	98.8	4.3	−0.12	0.10	0.47	99.0	4.1	−0.16	0.12	0.64	99.4	8.3	11.09	95.48	1	[+90.0,+105.6]	4(CO)	1667
G29.957−0.018	8.2	2.7	−0.06	0.03	0.07	7.8	2.6	−0.11	0.05	0.17	7.4	1.7	1.31	1.61	0	[+2.0, +13.0]	1667	1667
	–	–	–	–	–[c]	99.8	5.1	−0.08	0.04	0.19	98.0	7.2	13.33	101.98	1	[+93.0,+107.0]	4(CO)	4(CO)
G30.535+0.021	–	–	–	–	–[c]	43.7	4.7	−0.05	0.07[a]	–[b]	–	–	–	–	1	–	2(OH)	2(OH)
	–	–	–	–	0.28	49.4	3.5	−0.04	0.06[a]	0.57	47.7	4.4	4.96	42.44	1	[+33.0, +54.0]	2(OH)	2(OH)
	91.0	5.6	−0.06	0.11	0.67	92.1	5.4	−0.08	0.12	0.74	91.9	6.4	3.57	22.10	1	[+86.9, +98.0]	5(OH)	1667
G30.720−0.083*	93.1	5.8	−0.25	0.80	–[c]	94.1	5.8	−0.34	1.29	–[c]	94.0	9.2	8.36	73.81	1	[+87.0,+101.0]	7	7
G30.783−0.028	–	–	–	–	–	77.9	3.4	−0.13	0.04	–[b]	–	–	–	–	1	–	3(OH)	3(OH)
	81.6	6.3	−0.14	0.02	0.20	82.2	2.5	−0.44	0.11	0.39	81.9	5.6	2.30	12.18	1	[+79.0, +85.6]	4(CO)	1667
	87.1	2.7	−0.06	0.02	–[b]	–	–	–	–	–	–	–	–	–	1	–	3(OH)	3(OH)
	92.0	3.5	−0.25	0.07	0.39	92.2	3.5	−0.32	0.09	0.55	93.3	8.7	7.41	70.82	1	[+85.0,+103.0]	4(CO)	1667
	98.3	3.4	−0.07	0.01	–[b]	98.8	4.2	−0.10	0.03	–[b]	104.9	5.6	1.78	–[b]	1	–	3(OH)	3(OH)
G30.854+0.151	95.5	2.9	−0.14	0.52	1.36	95.3	3.2	−0.16	0.63	2.01	95.5	4.1	6.72	27.98	1	[+91.0, +98.5]	1667	1667
G31.242−0.110	–	–	–	–	–[c]	19.6	2.6	−0.12	0.26	0.83	20.8	3.8	3.33	12.45	1	[+15.0, +23.0]	1667	1667
	79.4	4.1	−0.07	0.15	0.57	78.9	2.5	−0.11	0.25	0.65	78.8	4.0	3.09	12.57	0	[+75.0, +81.8]	4	1667
	–	–	–	–	<0.29	83.7	2.5	−0.07	0.14	0.30	84.0	2.4	1.96	5.34	0	[+81.8, +87.1]	4	1667
G31.388−0.383	18.4	2.5	−0.08	0.06	0.17	17.9	2.5	−0.11	0.09	0.20	–	–	–	<1.79	0	[+15.0, +22.0]	2(CO)	1667
G32.151+0.132	93.8	6.0	−0.10	0.19	1.20	–	–	–	–	–	94.4	4.5	7.24	33.72	1	[+88.0,+101.0]	1665	1665
G32.272−0.226	22.6	4.6	−0.06	0.19	0.91	–	–	–	–	–	22.4	5.7	1.20	6.76	1	[+18.0, +27.0]	4(CO)	1665
G32.798+0.190	12.8	11.8	−0.17	0.12	1.45	–	–	–	–	–	15.1	7.4	6.61	51.69	1	[+0.0, +25.0]	1665	1665
G32.928+0.607	−33.9	2.9	−0.05	0.21[a]	0.64	–	–	–	–	–	–	–	–	–	1	[−41.0, −28.0]	1	1
G33.915+0.110	95.3	3.4	−0.04	0.06[a]	0.16	–	–	–	–	–	–	–	–	<2.28	1	[+92.0, +96.5]	2(OH)	2(OH)
	101.5	2.9	−0.06	0.08[a]	0.28	–	–	–	–	–	–	–	–	<2.28	1	[+96.5,+104.0]	2(OH)	2(OH)
	106.3	2.7	−0.11	0.16	0.46	–	–	–	–	–	107.5	4.6	6.80	32.47	1	[+103.4,+113.0]	1665	1665
G34.132+0.471	33.8	3.1	−0.08	0.17	0.59	–	–	–	–	–	35.1	3.8	2.93	11.88	1	[+28.0, +39.5]	1665	1665
G35.467+0.139	77.0	2.9	−0.07	0.32	0.86	–	–	–	–	–	77.4	3.2	8.73	29.92	1	[+74.0, +80.1]	1665	1665
G37.764−0.215	63.4	4.3	−0.32	0.28	1.64	–	–	–	–	–	61.5	5.6	3.29	35.33	1	[+56.5, +69.5]	4	1665
G37.874−0.399	61.0	10.1	−0.31	0.19	1.91	–	–	–	–	–	61.4	7.2	4.29	32.56	1	[+52.5, +67.5]	5(OH)	1665
G38.876+0.308	−16.4	2.9	−0.07	0.38	1.03	−16.1	4.1	−0.08	0.48	1.79	–	–	–	–	1	[−20.0, −13.0]	1	1
G39.565−0.040	23.4	2.8	−0.10	0.24	0.66	23.1	2.5	−0.15	0.37	0.96	23.4	3.1	1.25	4.65	0	[+17.0, +28.0]	1667	1667
G39.883−0.346	56.9	4.8	−0.05	0.23	1.23	56.9	3.5	−0.09	0.45	1.50	58.7	4.6	4.60	23.11	1	[+50.5, +63.5]	1667	1667
G41.741+0.097	14.4	8.2	−0.04	0.17	0.47	13.9	4.3	−0.05	0.18	0.52	13.4	2.9	2.44	5.79	1	[+10.0, +14.2]	5(OH)	1667
G42.027−0.604	–	–	–	–	<0.33	65.1	3.5	−0.05	0.14	0.59	65.5	3.9	3.02	12.48	0	[+62.0, +71.0]	4(CO)	1667
G45.454+0.060	–	–	–	–	–	56.0	7.2	−0.17	0.07	–[b]	–	–	–	–	1	–	3(OH)	3(OH)
	59.3	4.1	−0.19	0.07	–[c]	59.5	2.5	−0.38	0.18	0.83	58.9	5.9	8.02	45.42	1	[+53.2, +62.3]	4(CO)	1667
	–	–	–	–	–	64.9	8.2	−0.09	0.03	–[c]	–	–	–	–	1	–	3(OH)	3(OH)
G49.206−0.342	65.3	6.4	−0.52	0.24	1.79	–	–	–	–	–	65.7	6.0	4.31	28.54	1	[+55.0, +73.0]	1665	1665
G49.369−0.302	50.9	4.4	−0.75	0.24	1.26	–	–	–	–	–	51.1	4.5	11.71	61.22	1	[+44.5, +57.5]	1665	1665
	62.9	5.2	−0.33	0.11	0.63	–	–	–	–	–	61.1	2.3	4.11	24.18	1	[+56.5, +69.5]	4	1665
G49.459−0.353	62.0	7.4	−0.36	0.10	0.68	–	–	–	–	–	61.1	8.2	4.55	34.25	1	[+55.0, +65.0]	4	1665
	68.6	3.7	−0.81	0.22	1.01	–	–	–	–	–	68.6	4.7	7.47	40.51	1	[+65.0, +73.0]	1665	1665
G49.488−0.380	65.9	2.5	−1.89	0.18	0.48	–	–	–	–	–	67.8	4.0	6.13	44.89	1	[+63.0, +72.5]	4	4
G52.753+0.334	13.6	2.9	−0.02	0.07[a]	<0.35	10.6	4.8	−0.04	0.12	0.31	15.2	2.3	2.86	7.22	1	[+11.5, +18.5]	7	7
	45.3	2.5	−0.01	0.04[a]	<0.32	45.0	2.5	−0.05	0.14	0.36	44.5	2.8	2.00	5.18	0	[+43.0, +47.0]	5(OH)	1667
G60.882−0.132	22.3	3.7	−0.06	0.19	0.70	22.3	4.2	−0.08	0.30	1.35	22.4	3.9	28.61	116.83	1	[+17.0, +28.0]	1667	1667
G61.475+0.092	–	–	–	–	<0.03	5.9	4.2	−0.04	0.05[a]	0.05	6.6	0.7	1.86	0.49	(0)	[+2.5, +10.0]	2(OH)	2(OH)
	21.2	2.5	−1.38	0.40	1.22	21.1	2.5	−1.77	0.51	1.66	21.6	3.6	31.29	118.42	1	[+17.5, +25.0]	1667	1667

Notes. Gaussian profiles are fitted to the OH 1665 MHz and OH 1667 MHz absorption spectra to determine the central velocity (v), the full width of half maximum (Δv) and the minimum line depth ($F_{\rm peak}$). Similarly, the line parameters of the ^{13}CO emission are determined. The peak optical depth ($\tau_{\rm peak}$) is determined by fitting Gaussians to the optical depth spectra. The velocity integrated optical depth ($\int\tau{\rm dv}$) and ^{13}CO emission is determined by summing all channels over a common range of OH absorption and ^{13}CO emission (Column "Int. Range"). For lines that were not detected, 3-σ upper limits ("<") are given under the assumption of an average line width of 3.6 km s^{-1} for the OH 1665 MHz transition and 4.0 km s^{-1} for the ^{13}CO transition. Notes on each detection indicate if the OH transition at 1665 MHz or at 1667 MHz ("1665"/"1667") was used for the linewidth comparison ("FWHM"; Fig. 6) or the OH abundance ("Int."; Figs. 7, 8, 9 and 13). Numbers specify why a transition was not used: (1) No ^{13}CO data available; (2) Weak or non-detection; (3) Auxiliary fit component; (4) Blended components could not be separated; (5) Bad fit; (6) No velocity overlap between OH and ^{13}CO; (7) OH spectrum affected by emission of a maser at this position or close-by.

Footnotes: [(a)] 3-σ detection; [(b)] Included in integration of an adjacent component; [(c)] This transition is affected by emission of a maser at this position or close-by; [(*)] Data at 20″ resolution was used in order not to blend with an adjacent maser.

tional emission observations were obtained at a position slightly offset from the continuum source. The OH emission is not detectable in the present dataset, as the OH emission is expected to be dominated by warm gas (e.g., Wannier et al. 1993) that varies on scales larger than the interferometric observations presented here. Hence, emission is filtered out. Observations of transitions to higher rotational levels of OH are not available for most sources and would require detailed modelling to constrain the excitation conditions of the hyperfine transitions in the ground state, which is beyond the scope of this paper. We therefore assume an excitation temperature from the literature in order to determine OH column densities (e.g., Stanimirović et al. 2003).

The excitation temperatures of the OH main lines have been found to differ relative to each other by 0.5 – 2.0 K (e.g., Goss 1968; Crutcher 1979; Dawson et al. 2014). This has also been seen in models (e.g., Guibert et al. 1978). The level populations may also be affected by radiative pumping (Csengeri et al. 2012; Wiesemeyer et al. 2016). Previous investigations reported excitation temperatures for the OH main line transitions between 3 and 10 K (e.g., Goss 1968; Turner 1973; Crutcher 1977; Colgan et al. 1989; Li & Goldsmith 2003; Bourke et al. 2001; Yusef-Zadeh et al. 2003). We therefore assume a uniform excitation temperature of $T_{\rm ex}(1665) = 5$ K for the 1665 MHz transition, which in principle can be higher by up to about a factor of two for OH gas associated with H II regions. We consider this in the systematic uncertainties (see Sect. 3.2.5). For transitions in which both main lines are detected, the medians of the column density distributions of each main line are offset. A better agreement between the samples is reached for a slightly higher excitation temperature for the 1667 MHz line of $T_{\rm ex}(1667) = 6.7$ K . We therefore adopt this value for the OH 1667 MHz transition in the following, while using $T_{\rm ex}(1665) = 5$ K in the OH 1665 MHz transition.

3.2.3. H_2 column density

As proxy for H_2, we use ^{13}CO emission. Kinematically, ^{13}CO is related to the OH gas. The line widths of the OH main lines and ^{13}CO are compared in Fig. 6. The channel spacing of 1.5 km s^{-1} in the OH observations poses a limit of 2.5 km s^{-1} on the narrowest resolved line width for OH lines, while the full spectral resolution of 0.25 km s^{-1} is used for ^{13}CO to disentangle different velocity components. Excluding the unresolved OH lines, the line widths of both tracers are found to be correlated[4]. In some cases, the ^{13}CO emission features larger line widths than OH. One possible explanation is that larger parts of the molecular cloud contribute to the ^{13}CO antenna temperature than to the OH absorption. For many continuum sources, only OH absorption from scales less than 46" is recovered. As emission from within the entire beam contributes to the ^{13}CO antenna temperature, the ^{13}CO emission may average over larger parts of the cloud. Similarly, if the continuum source is located within the molecular cloud, ^{13}CO emission contains information from all cloud depths (if not optically thick), while only parts of the cloud between the continuum source and the observer affect the OH absorption (see also sect. 3.2.5). Depending on the velocity substructure of the cloud on scales smaller than the beam and along the line of sight, this can lead in both cases to larger line widths in the ^{13}CO emission than in the OH absorption.

[4] This sample of 15 datapoints is described by a Pearson's correlation coefficient $\rho = 0.8$ at a statistical significance of $\approx 3\sigma$.

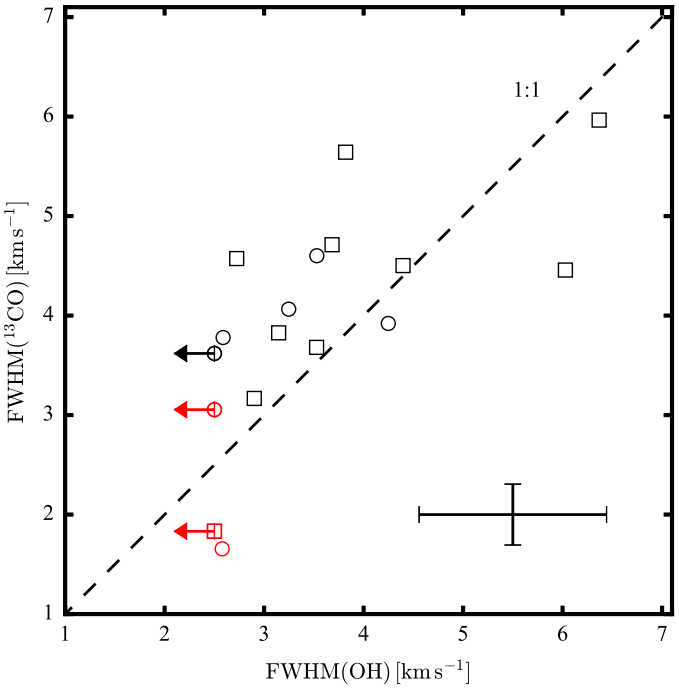

Fig. 6. Comparison of FWHM of OH and ^{13}CO(1-0) lines. OH line widths of the 1665 MHz transition (upper panel, squares) are used whenever the 1667 MHz transition (lower panel, circles) was not available. Detections associated with H II regions are drawn in black, others in red. Arrows indicate spectrally unresolved lines. The dashed line indicates a 1:1 correlation. The bars in the lower right-hand corner of the figure indicate typical errors in both quantities.

The column density of ^{13}CO is determined from the integrated line profile ($\int T_{\rm mb} {\rm dv}$) under the assumption that the gas is optically thin (e.g., Wilson et al. 2009, eq. 15.37) :

$$N(^{13}{\rm CO}) \approx 3.0 \times 10^{14} \frac{\int \frac{T_{\rm mb}}{\rm K} {\rm dv}}{1 - \exp\left(-5.3/T_{\rm ex}\right)} {\rm cm}^{-2}. \quad (3)$$

Average excitation temperatures of ^{13}CO in molecular clouds are typically between 10–15 K, with values of up to 25 K in some cases (e.g., Pineda et al. 2010; Nishimura et al. 2015; Frerking et al. 1982; Anderson et al. 2009). We select an excitation temperature towards the upper end of this range of $T_{\rm ex} = 20$ K, as most of the OH detections are associated with H II regions. To account for possibly lower excitation temperatures, we assume an uncertainty of a factor of two on $T_{\rm ex}$, which results in an uncertainty of approximately a factor of two for $N_{^{13}{\rm CO}}$.

The column density of molecular gas is determined by assuming a constant ^{13}CO abundance relative to molecular hydrogen molecules of $N_{\rm H_2}/N_{^{13}{\rm CO}} = 3.8 \times 10^5$ (Bolatto et al. 2013; Pineda et al. 2008). Uncertainties in this estimate due to optical thickness of ^{13}CO or local variations in the ^{13}CO/^{12}CO ratio (Szűcs et al. 2016) are discussed in Sect. 3.2.5. If the ^{13}CO(1 – 0) emission is not detected, we report upper limits for both $N_{\rm H_2}$ and $N_{\rm H}$ and lower limits on $X_{\rm OH}$.

3.2.4. H I column density

To derive the H I column density, we assume a spin temperature (= $T_{\rm ex}$) of $T_{\rm spin} \sim 100$ K (Bihr et al. 2015). The H I column density is given by (e.g., Wilson et al. 2009)

$$N_{\rm H\,I} = 1.8224 \times 10^{18} \frac{T_{\rm spin}}{\rm K} \int \tau({\rm v}) \left(\frac{\rm dv}{\rm km\,s^{-1}}\right) {\rm cm}^{-2}. \quad (4)$$

Since the optical depth is a lower limit here (see sect. 3.2.1), the H I column density is a lower limit as well. As $T_{\rm spin}$ may vary for individual regions by a factor of two, these limits are subject to a systematic uncertainty of the same factor.

In the following, we determine the OH abundance, $X_{\rm OH}$, both in terms of the column density of molecular hydrogen, $N_{\rm H_2}$, and in terms of the total column density of hydrogen nuclei, which includes both atomic and molecular hydrogen, $N_{\rm H\,I}$ and $N_{\rm H_2}$. $N_{\rm H}$ is given by $N_{\rm H} = N_{\rm H\,I} + 2N_{\rm H_2}$. The lower limits on $N_{\rm H\,I}$ yield upper limits on $X_{\rm OH}$. The derived quantities from this section are listed in Table 3.

3.2.5. Systematic uncertainties

The systematic uncertainties of $X_{\rm OH}$, $N_{\rm H_2}$ and $N_{\rm H}$ are estimated as follows. The $N_{\rm H_2}/N_{\rm ^{13}CO}$ ratio varies within molecular clouds and may be affected by global changes in the ^{13}C isotope abundance with Galactocentric radius. First, the scatter of $N_{\rm H_2}/N_{\rm ^{13}CO}$ measurements has been found to be up to a factor of two within individual clouds (e.g., in Perseus; Pineda et al. 2008). We assume that this inflicts an uncertainty of a factor of two on $N_{\rm H_2}$. Second, the conversion used here has been determined in nearby Gould Belt clouds, but the ^{12}C/^{13}C isotope ratio increases with Galactocentric radius (Milam et al. 2005). With absorption sources located at Galactocentric radii between $R_{\rm gc} = 3-10$ kpc, we assume that global variations in the ^{13}C isotope abundance introduce an additional uncertainty of a factor of two on $N_{\rm H_2}$.

As described above, the assumptions regarding the excitation temperatures of OH, ^{13}CO(1-0) and H I are likely to be valid within a factor of two as well. These result in a combined uncertainty of approximately a factor of 3.5 in $N_{\rm H_2}$ and $N_{\rm H}$, and a factor of four in $X_{\rm OH}$. As the H I absorption saturates in most cases, we can only determine lower limits to $N_{\rm H\,I}$.

Also, some of the ^{13}CO$(1-0)$ emission may be optically thick and give lower limits on $N_{\rm H_2}$, and therefore upper limits on $X_{\rm OH}$. While $N_{\rm H_2}$ as derived from ^{13}CO may also be underestimated due to chemical effects (e.g., Szűcs et al. 2016), the derived H_2 column densities have been compared with column densities derived from 870 μm dust emission (ATLASGAL), and we find reasonable agreement also towards high column densities within a factor of two.

At low CO column densities, molecular cloud regions may be traced that contain a significant fraction of "CO-dark" H_2. This means that the column density of H_2 would be underestimated and the OH abundance overestimated. The amount of "CO-dark" gas depends on the environment, i.e., on metallicity and the strength of the external radiation field. This makes a quantitative correction difficult, but the effect may influence detections for which H_2 and H I column densities are comparable.

Geometrical uncertainties should also be considered. For the sake of simplicity, they are mentioned here only briefly, because they are difficult to quantify. First, the ^{13}CO emission may trace molecular gas that is not accessible by the OH absorption observations. OH absorption occurs in material between the observer and a continuum source, while material at any distance along the sightline contributes to the ^{13}CO emission if optically thin. Most of the OH absorption detections are associated in velocity with the continuum source itself and by our definition separated from the continuum source by less than 10 km s^{-1}. Assuming that the OH and ^{13}CO gas, as well as the H II-region are part of the same molecular cloud, a fraction of the ^{13}CO emission emerges from behind the continuum source as seen by the observer. This fraction depends on the structure of the molecular cloud and the relative position of the continuum source. For example, 50% of the ^{13}CO emission will come from behind the H II region, if it is embedded in the middle of a spherically symmetric molecular cloud. No OH absorption can be measured for this part of the cloud, and the OH abundance will be underestimated. Velocity shifts between the different tracers in our data (<2 km s^{-1}) indicate that at least some sources are affected by this. As we cannot constrain the structure of the cloud and quantify this effect, we choose not to correct for it here.

Second, crowded regions may contain multiple, overlapping H II-regions, which contribute to the observed continuum flux, if the continuum emission is optically thin. If OH absorption occurs along the line of sight in between such continuum sources, the observed continuum will overestimate the true continuum incident on the absorbing cloud. Therefore, the optical depth of OH would be underestimated. This is likely to affect lines of sight towards galactic continuum sources that are located in crowded regions, such as the tangent points of spiral arms (G29, W43 and W51).

3.2.6. OH vs. H_2 column density

OH and H_2 column densities are shown in Fig. 7. $N_{\rm OH}$ is derived from the 1667 MHz transition (circles) if available, and from the 1665 MHz transitions in the rest of the cases (squares). The absorption features are separated by color into regions that are associated (black) or not associated (red) with H II regions.

To investigate the correlation between $N_{\rm OH}$ and $N_{\rm H_2}$, we perform a linear regression in log-space, $\log(N_{\rm OH}) = m \times \log(N_{\rm H_2}) + t$, to determine the slope m. The uncertainties are dominated by the systematic errors, i.e. possible variations of $N_{\rm OH}$ and $N_{\rm H_2}$ by a factor of 2 and 3.5, respectively (see sect. 3.2.5). To properly take into account their impact on the correlation, we estimate the distribution of slopes m given these uncertainties and the stochastic measurement errors. We do not include upper limits. We sample the *posterior* distribution of m by performing linear regressions on multiple, artificial representations of the data, which are inferred from the uncertainty distributions of the measurements.

We create a large number of artificial datasets ($n_{\rm datasets} = 10^5$). Each artificial dataset has the same number of points as our measured sample, but instead of containing the measurements itself, each point is replaced by randomly drawing an artificial datapoint from the uncertainty distribution. We also "bootstrap" each of these simulated dataset, i.e. randomnly assigning weights to the points to reduce the importance of each individual measurement. From the linear regression on each of these artificial dataset, we obtain a distribution of slopes with median and 16%-, 84%-percentiles of $m = 0.32^{+0.13}_{-0.13}$ (see also Fig. B.1). The green line in Fig. 7 shows the median slope.

We interpret this result as an indication of a weak, sublinear correlation between $N_{\rm OH}$ and $N_{\rm H_2}$. A direct proportionality between the two parameters is unlikely, given the distribution of slopes. The sublinear relation between $N_{\rm OH}$ and $N_{\rm H_2}$ yields a decreasing OH abundance ($X_{\rm OH} = N_{\rm OH}/N_{\rm H_2}$), as discussed in the following sections. The analysis shows that a correlation is present in the data, but for tighter constraints, follow-up studies are needed to provide more data and/or to decrease the systematic uncertainties.

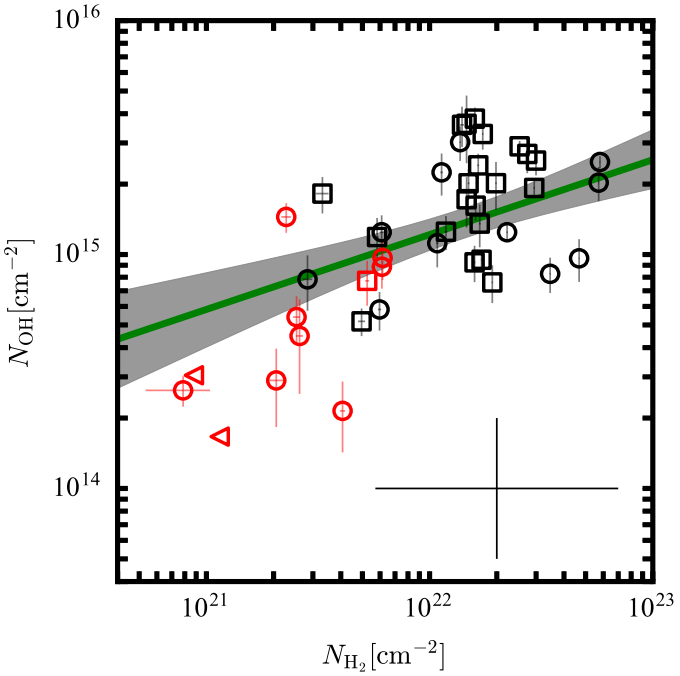

Fig. 7. Comparison of the OH column density from the 1665 MHz (squares) and 1667 MHz transitions (circles) to that of H_2 as inferred from ^{13}CO(1-0) emission. Column densities from absorption features overlapping in velocity with H II regions (black) and with no such counterpart (red) divide the plot into regions with higher and lower hydrogen column densities. Triangles denote upper limits on N_{H_2} as determined from ^{13}CO(1-0) non-detections. The green line is the result of parameter estimation of a correlation between N_{OH} and N_{H_2}, using errors on x and y axes and not including upper limits. The gray shaded regions shows the 16%- and 84%-percentiles. The black error bars in the lower right corner show the systematic errors.

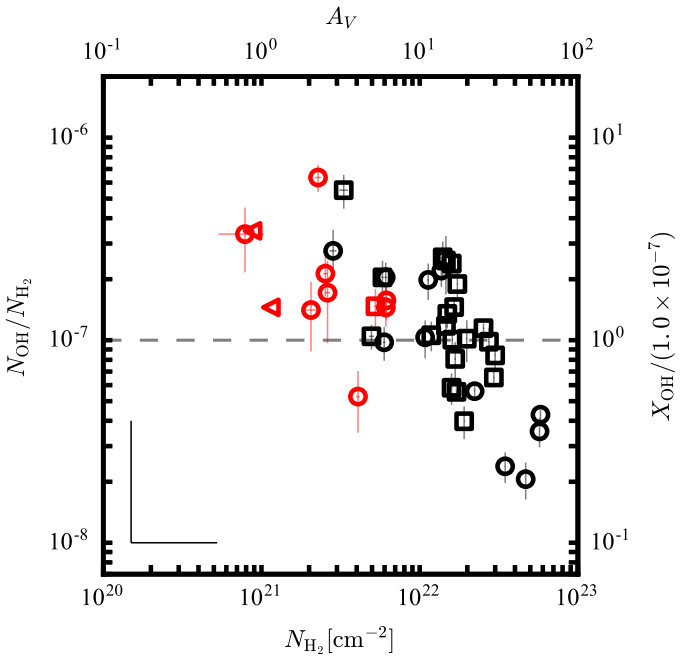

Fig. 8. OH abundance $X_{OH} = N_{OH}/N_{H_2}$ vs. N_{H_2}. N_{OH} is inferred from 1665 MHz (squares) or 1667 MHz absorption (circles) and N_{H_2} from ^{13}CO(1-0) emission. Absorption features associated with H II regions are shown in black; those not associated are shown in red. Triangles denote upper limits on N_{H_2} (inferred from the non-detection of ^{13}CO). The right axis shows the OH abundance in units of literature (molecular) OH abundance of 1×10^{-7} (e.g., Liszt & Lucas 1999, 2002, indicated also by the dashed gray line). The black error bars in the lower left corner show the systematic errors (only the upper halfs of the error bars are shown here).

3.2.7. OH abundance at different hydrogen column densities

Fig. 8 shows the OH abundance in terms of the molecular hydrogen column density ($X_{OH} = N_{OH}/N_{H_2}$) versus N_{H_2}. The literature value for $X_{OH} = N_{OH}/N_{H_2} \approx 1 \times 10^{-7}$ is plotted as a dashed gray line, and the right axis shows the data in terms of this value (e.g., Guelin 1985; Langer & Graedel 1989; van Langevelde et al. 1995; Liszt & Lucas 1999, 2002). The OH abundance is found to be anti-correlated with N_{H_2} over the range of probed cloud depths ($8 \times 10^{20}\,{\rm cm}^{-2} < N_{H_2} < 5.8 \times 10^{22}\,{\rm cm}^{-2}$). Above $N_{H_2} > 1.9 \times 10^{22}\,{\rm cm}^{-2}$ ($A_V \sim 20$ mag)[5], most of the abundances are lower than the literature value, while the abundances at lower H_2 column densities are slightly higher.

We use the H I absorption data as lower limit for the column density of atomic hydrogen, and show the OH abundance with respect to the total number of hydrogen nuclei in Fig. 9. While the overall trend is similar to that seen in Fig. 8, the atomic hydrogen content probed along the line-of-sight is comparable to molecular hydrogen for a few detected components with low molecular hydrogen column densities (e.g., for G29.935−0.053 at 7.0 km s^{-1} and G29.957−0.018 at 8.0 km s^{-1}).

[5] Assuming $N_H/(A_V/R_V) = 5.8 \times 10^{21}\,{\rm cm}^{-2}\,{\rm mag}^{-1}$ (Bohlin et al. 1978) and the average ISM value for the total-to-selective extinction of $R_V = 3.1$, the total hydrogen column density can be related to visual extinction as $N_H = 1.9 \times 10^{21}\,{\rm cm}^{-2}\,{\rm mag}^{-1} \times A_V$. For large column densities ($N_{H_2} \gg 5 \times 10^{21}\,{\rm cm}^{-2}$) we assume the contribution of atomic hydrogen to be negligible, i.e., $N_H \approx 2 \times N_{H_2}$.

We see a clear anti-correlation between X_{OH} and N_{H_2} for OH associated with H II regions (black). Measurements which are not associated (red), follow this trend in Fig. 8. In the abundance with respect to all hydrogen nuclei (N_{OH}/N_H) in Fig. 9, this trend appears not to be present in the red data points, since the lowest data points have significant contribution from atomic hydrogen. As the H I column densities are lower limits, the abundances are upper limits, favoring an even shallower trend of X_{OH} in this N_H column density regime. As mentioned in Sect. 3.2.5, also the fraction of "CO-dark" H_2 may be significant for most of the detections which are not associated with H II regions and the lowest of the measurements associated with H II regions, which would place them at higher N_{H_2} (and N_H) and lower X_{OH} in Figs. 8 and 9.

The red data points fall into similar ranges of visual extinction as probed by many earlier studies. The OH abundance for visual extinctions of $A_V < 7$ mag has been reported in the literature to be constant at $X_{OH} = N_{OH}/N_H = 4 \times 10^{-8}$ (e.g., Goss 1968; Crutcher 1979). The median OH abundance for this group of points here is $X_{OH}(N_{H_2}) = 1.6 \times 10^{-7}$ with a scatter of $\Delta X_{OH} = 0.27$ dex and $X_{OH}(N_H) = 6.0 \times 10^{-8}$ and a scatter of $\Delta X_{OH} = 0.22$ dex.

3.3. Satellite line transitions

Satellite lines of the OH ground state transitions are rarely found in local thermodynamic equilibrium with the main line transitions. While the main lines are seen in absorption, the satellite lines can be anomalously excited and may show conjugate emission and absorption, often at equal strength (e.g., towards

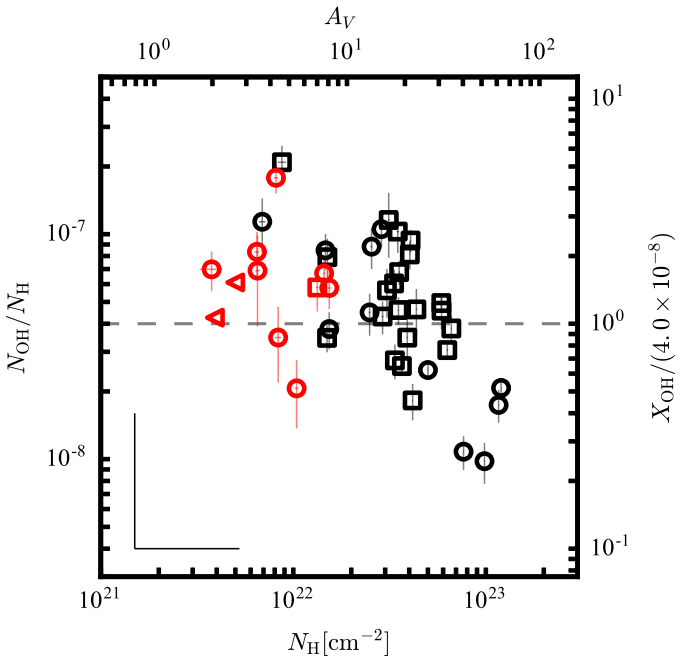

Fig. 9. OH abundance $X_{OH} = N_{OH}/N_H$ vs. N_H. The total column density of hydrogen nuclei, N_H, is inferred from ^{13}CO(1-0) emission and H I absorption. As the H I column density represents lower limits, the OH abundances represent upper limits. Colors and symbols are as in Fig. 8. The right axis shows the OH abundance in units of the typical OH abundance in diffuse clouds of 4×10^{-8} (Crutcher 1979, indicated also by the dashed gray line).

G18.303−0.390 and G25.396+0.033; see Fig. C.1). Table 4 catalogs conjugate satellite transitions found in this survey. The qualitative satellite line behavior reflects the physical conditions of the gas, such that we can use this to estimate OH column densities for a subsample of sources.

Emission in the 1612 MHz transition with absorption in the 1720 MHz transition is found in 14 instances. Emission in the 1720 MHz transition with absorption in the 1612 MHz transition occurs in three cases (e.g., towards G32.798+0.190 at 90 km s^{-1}; see Table 4).

Satellite line reversal, i.e., the transition from absorption to emission (or vice versa) across the line, is seen along 3 lines of sight. Both satellites mirror each other: At lower velocities, the 1720 MHz line is in emission, while the 1612 MHz line is in absorption. At a certain velocity, the behavior reverses. This is found in the following cases in this work: G19.075−0.288 at 67.5 km s^{-1}, G32.798+0.190 at 14.0 km s^{-1}, G49.369−0.302 at 63.5 km s^{-1}. Lines of sight, for which the full reversal profile is not detected in both satellite lines, but which are indicative of this behavior, are: G29.935−0.053 at 98.5 km s^{-1}, for which reversal in the 1612 MHz transition is detected, but the 1720 MHz line is seen only in absorption at higher velocities, and not detected in emission at lower velocities. Towards G37.764−0.215 at 65.0 km s^{-1}, G49.206−0.342 at 63.5 km s^{-1} and G49.369−0.302 at 49.5 km s^{-1}, 1612 MHz absorption is seen at low velocities without conjugate emission in the 1720 MHz transition, while at higher velocities, the 1720 MHz transition is in absorption without conjugate emission in the 1612 MHz transition.

In the other cases, the satellite lines are not detected or only one transition of the two is detected. Indication of absorption in both lines can be seen in G61.475+0.092 at +21.2 km s^{-1}, with the satellite line strengths differing from each other, as is expected since the lines are typically not in local thermal equilibrium.

The conjugate emission and absorption of the satellite lines has been noted in previous studies (e.g., Goss 1968; Crutcher 1977; van Langevelde et al. 1995; Brooks & Whiteoak 2001; Dawson et al. 2014), and is the result of overpopulation of either the F=1 or the F=2 hyperfine energy levels of the ground state and mutual depletion of the others (e.g., Elitzur 1992, §9.1). As the satellite lines are transitions with $|\Delta F| = 1$, they are affected by the relative population changes, while the main line transitions with $|\Delta F| = 0$ may not be affected by this particular inversion mechanism.

There are different pumping mechanisms that may be responsible for the population inversion (see discussion in, e.g., Frayer et al. 1998). In all cases, transitions from higher rotational levels to the ground state need to become optically thick (e.g., Elitzur 1992; van Langevelde et al. 1995): If the infrared transitions from either the $^2\Pi_{3/2}(J = 5/2)$ or the $^2\Pi_{1/2}(J = 1/2)$ states into the ground state become optically thick, the 1720 MHz or the 1612 MHz transition, respectively, is seen in inversion. If both transitions are optically thick, inversion of the 1612 MHz transition is seen. As the transitions from the $^2\Pi_{3/2}(J = 5/2)$ excited state become optically thick at lower N_{OH} than from the $^2\Pi_{1/2}(J = 1/2)$ state, there exists a typical OH column density at which the transition from 1720 MHz to 1612 MHz inversion takes place. This has been used and modeled by van Langevelde et al. (1995) for a molecular cloud heated by a background H II region and satellite line reversal was found to take place at $\approx 1\times10^{15}$ cm^{-2} km^{-1} s.

Assuming this geometry also for the sources in this sample, this model provides a possibility to estimate N_{OH}. The column density depends on the velocity dispersion of the gas ($N_{OH} \approx \Delta v \times 1\times10^{15}$ cm^{-2} km^{-1} s). As we have no direct measure of the line width at the velocity of the reversal of the inversion we use as approximation the full width of half maximum of the 1665 MHz main. The transition occurs at $N_{OH} \approx 7.4\times10^{15}$ cm^{-2} for G19.075−0.288, at $N_{OH} \approx 1.2\times10^{16}$ cm^{-2} for G32.798+0.190 and at $N_{OH} \approx 4.4\times10^{15}$ cm^{-2} for G49.369−0.302.

We compare the estimates for G32.798+0.190 and G49.369−0.302 to N_{OH} derived from the main lines in Sect. 3.2. G19.075−0.288 is omitted here, as the reversal velocity does not match the velocity of the maximum optical depth of the 1665 MHz transition (Fig. C.1). For G32.798+0.190 and G49.369−0.302, N_{OH} determined from the main lines is a factor of 3–4 lower than the estimate from the satellite lines. The line width used for the N_{OH} estimate from the satellite lines could be an overestimate if multiple components are blended into the feature. Alternatively, the discrepancy could be an indication of higher main line excitation temperatures than the assumed $T_{ex}(1665) = 5$ K. To match the estimates from the satellite lines, excitation temperatures of $T_{ex} \approx 15 - 20$ K would be required.

A similar discrepancy has been noted in Xu et al. (2016), who find lower OH column densities than needed to reproduce the observed emission in the 1612 MHz transition. They attribute this to other excitation mechanisms, such as collisional excitation in shocks (e.g., Pihlström et al. 2008), which are not taken into account in the model by van Langevelde et al. (1995).

Recently, employing non-LTE modeling of all four 18 cm OH emission lines, Ebisawa et al. (2015) have used the relative intensities of main-line and 1720 MHz emission and 1612 MHz absorption in the Heiles Cloud 2 and ρ Oph to derive kinetic temperatures that are significantly higher in translucent than in dark

molecular regions. This indicates that OH appears to be able to probe the interface between molecular and warmer atomic material. Such an analysis is beyond the scope of the present paper, but can be included in a future study.

3.4. Extended OH absorption: the example of W43

Spatially resolved OH absorption is seen against a subsample of the continuum sources (examples of these are the Galactic H II regions M17, G18.148−0.283, G37.764−0.215, G45.454+0.060 and G61.475+0.092). This allows for a comparison of column density and kinematic structure in different physical regimes: The ionized gas phase is traced by continuum emission and RRLs, the cold neutral medium is traced by H I absorption and the molecular gas regime is traced by different CO isotopologues and far-IR continuum emission. We present the star-forming region W43, as an example of what can be learned from this data.

W43 is one of the largest molecular cloud complexes in our Galaxy. It is located at the intersection of the Scutum-Centaurus spiral arm with the Galactic bar, is actively forming stars at a high rate and is dynamically complex (e.g., Nguyen Luong et al. 2011; Motte et al. 2014; Bihr et al. 2015). It is composed of multiple sub-regions, most prominently the W43-main and W43-south regions, which themselves break down into smaller regions of molecular gas (e.g., Carlhoff et al. 2013). In W43-main, complex structure is also indicated by the high H I column densities (e.g., Liszt 1995; Motte et al. 2014; Bihr et al. 2015), which suggests the presence of several molecular clouds along the line-of-sight (Bialy et al. 2017).

Different evolutionary stages of stars and clouds coexist and appear to be influencing each other: An OB cluster at the center of W43-main, which contains Wolf-Rayet stars, includes a strong source of ultraviolet photons (e.g., Smith et al. 1978; Blum et al. 1999); these provide the ionization and heating of the central H II region (e.g., Reifenstein et al. 1970; Lester et al. 1985). There is evidence for a second generation of star formation, indicated by clumps of dense gas and ultra-compact H II regions (e.g., Motte et al. 2003; Bally et al. 2010; Beuther et al. 2012), which conveys the picture of gas compression driven by the central H II regions (e.g., Blum et al. 1999; Balser et al. 2001). In the environment of W43-main, pre-stellar cores manifest higher gas temperatures than in quiescent regions due to the heating by the central cluster, possibly affecting the number of stars formed in the future (Beuther et al. 2012). Adding to the complexity of the region, observations of molecular and ionized gas tracers revealed several velocity gradients and substructures of different morphologies (e.g., Liszt 1995; Balser et al. 2001; Carlhoff et al. 2013). The gas streams on global scales in molecular and atomic gas indicate that the H to H_2 conversion is ongoing (Motte et al. 2014). Dynamical interaction between clouds has been investigated on smaller scales with SiO emission, which possibly emerges from low velocity shocks in mm-emission peaks (e.g., Nguyen Luong et al. 2013; Louvet et al. 2016).

The extended OH absorption in W43 is displayed in the left panel of Fig. 10, in which the optical depth has been integrated between 78.0–100.5 km s^{-1} and all maps are shown at an angular resolution of $20'' \times 20''$, corresponding to a spatial scale of 0.5 pc at a distance of 5.5 kpc (Zhang et al. 2014). Intrinsically, absorption is seen towards strong continuum emission peaks, as the sensitivity to find absorption increases with continuum emission strength. However, the strongest integrated optical depth peaks do not coincide with continuum emission peaks, but are seen towards the mm dust emission sources MM1 and MM3[6] (nomenclature taken from Motte et al. 2003). The integrated OH absorption varies by a factor of 3 around the central H II region, and is higher by an order of magnitude towards the outer parts of the T-shaped continuum emission: At MM3 and towards MM1, the total line-of-sight column density is approximately 7×10^{15} cm^{-2} and 9×10^{15} cm^{-2}, respectively while the column density is between $0.5 - 2 \times 10^{15}$ cm^{-2} around the central H II region, assuming an excitation temperature of $T_{\rm ex} = 5$ K in both cases.

Fig. 10 compares the optical depth of the OH 1667 MHz transition to ATLASGAL 870 μm dust emission (Schuller et al. 2009) and to $C^{18}O$(2–1) emission (Carlhoff et al. 2013). The middle panel displays the ratio of integrated OH optical depth to 870 μm dust emission, while the right panel displays the ratio to integrated $C^{18}O$(2–1) emission. Both the OH and $C^{18}O$(2–1) data have been integrated between 78.0 km s^{-1} and 100.5 km s^{-1}. For the OH optical depth only such pixels contribute to the integral that are significantly detected in the absorption data. The value of the ratio maps are shown for relative comparison of different parts of the region, motivated by the hypothesis that all the tracers are optically thin and hence contribute linearly to the column density of the species (the optical thickness of the tracers is discussed further in sect. 4.4). Thus, the ratios quoted here represent no physical quantity directly but their variation across the map can be indicative either of OH abundance or excitation variations.

The integrated $C^{18}O$ and 870 μm emission are shown as contours in Fig. 10. There are enhancements towards the central continuum source, towards MM1 and MM3 in both tracers. The strongest peak in the $C^{18}O$ emission is towards the central part of the T-bar, and is slightly offset from the peak of the continuum emission. The ATLASGAL emission peaks more strongly towards MM1 and MM3. At MM1, continuum emission and $C^{18}O$ emission are slightly shifted away from the 870 μm emission.

Within the central part of the T-bar, the ratio of OH optical depth to $C^{18}O$ emission is around 0.05, and slightly higher on the left side of the central continuum peak. This is similar in the 870 μm emission, where the ratio is between 0.2-0.3, and by a factor of 2 higher on the side facing MM1. The ratio is around a factor of 4-9 higher against the MM1 and MM3 sources in both tracers. This increase is slightly higher for the ratio to $C^{18}O$ emission than to 870 μm emission, which is consistent with the stronger increase of the 870 μm emission towards these sources. Against "Pos. 1", however, the ratio to ATLASGAL 870 μm emission is by a factor of ∼5 higher than in the central continuum emission region. The increase in this ratio is also seen in the $C^{18}O$ emission.

In order to understand this comparison better, Fig. 11 shows the ratio of OH optical depth and $C^{18}O$ in velocity ranges of 4.5 km s^{-1} (after binning three channels of 1.5 km s^{-1}). Between 81.0 and 84.0 km s^{-1}, OH absorption is seen against the central H II region and "Pos. 1". $C^{18}O$ is significantly detected only in few locations, and we include upper limits in the plot (encircled by blue contours). Ratios are found between 0.3 and 0.4. A similar ratio is seen between 90 km s^{-1} and 93.0 km s^{-1} towards MM3, MM1 and "Pos. 1". In this velocity range, however, the OH ratio at the center of the T-bar is rather low, between 0.03

[6] At MM3, the OH 1667 MHz absorption is affected by side lobes of close-by maser emission at 96 km s^{-1}. To determine the moment maps shown in Figs. 10 and 11, we interpolated over the channel at 96 km s^{-1} in lines of sight close to MM3. For clarity, this channel is masked in Fig. 12.

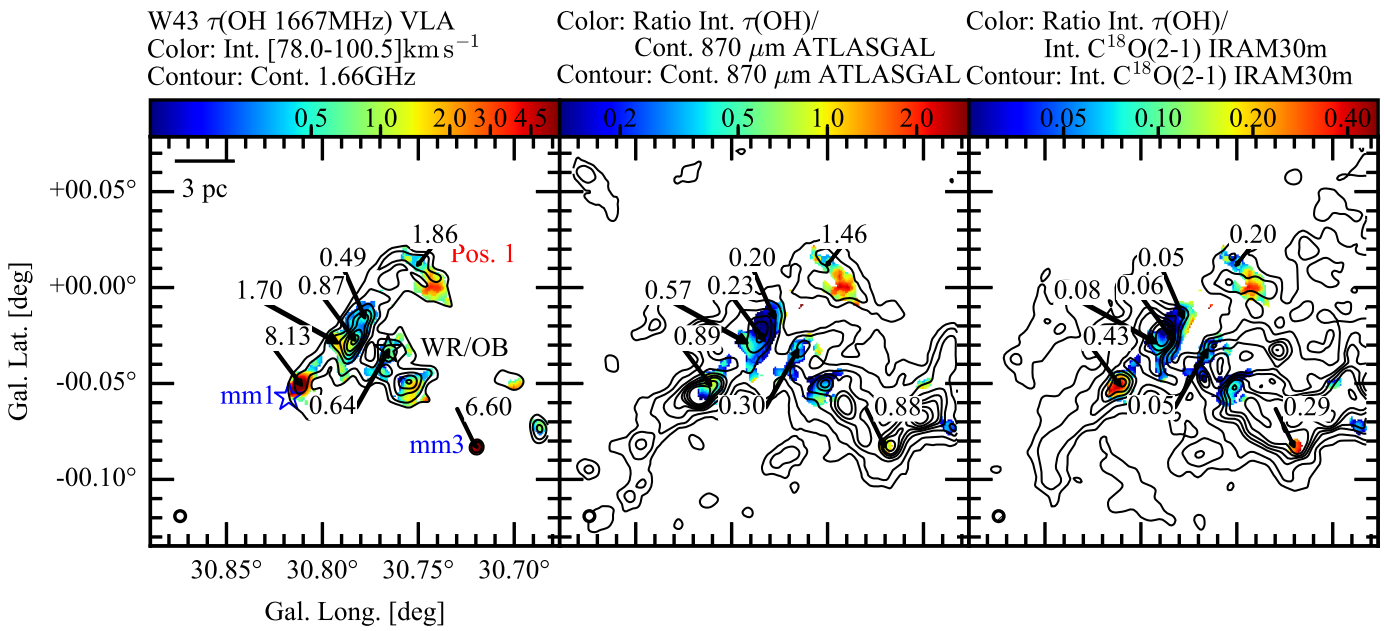

Fig. 10. Comparison of τ(OH 1667 MHz), dust continuum emission at $\lambda = 870\,\mu$m, and $C^{18}O$(2-1) emission in the W43 star-forming region. In the left panel, the integrated optical depth of the OH 1667 MHz transition between 78.0 and 100.5 km s^{-1} is displayed in colors. For each pixel, only channels that are detected at a 3-σ level contribute to the integrated τ-map. It is overlayed with contours of the 18 cm continuum emission (black, at levels of 0.1, 0.2, 0.4, 0.6, 0.8, 1.0, 1.25, 1.5 and 1.75 Jy beam^{-1}). The middle panel shows the ratio of the integrated τ(OH) map to 870 μm ATLASGAL emission (Schuller et al. 2009), which traces dense gas (the dust emission is overlayed in black contours, at levels of 0.5, 1.0, 2.0, 3.0, 4.0, 5.0, 7.0 and 10.0 Jy beam^{-1}). The right panel shows the ratio of τ(OH) to $C^{18}O$(2-1) emission (Carlhoff et al. 2013), integrated over the same velocity range (the velocity integrated $C^{18}O$(2-1) emission is overplotted in black contours at levels of 6, 9, 13, 15, 17, 19, 23 K km s^{-1}). All data have been smoothed to a common resolution of 20″, corresponding to spatial scales of 0.5 pc. In the top left panel, the central Wolf-Rayet/OB cluster is marked by a black star, while the dense clumps MM1 and MM3 (Motte et al. 2003) are marked by blue stars. The upper end of the T-bar-shaped continuum emission is marked as Pos. 1 for easier reference in the text. For readability, the values of the ratio are displayed for selected positions in the figure.

and 0.1. The ratio increases for MM1 towards 0.5 between 94.5 and 97.5 km s^{-1}.

To conclude, variations in OH to $C^{18}O$ ratio are seen also when refining the integration interval. There seem to be two regimes – the central part of the H II region exhibits a ratio of ∼ 0.05, while for other locations and other velocities, we find a ratio of ∼ 0.3. At lower velocities, also the central part of the H II region is seen at ratios of ∼ 0.3. This is further discussed in Section 4.4.

4. Discussion

4.1. Distribution of OH in the Galactic plane

Recent single-dish observations of the OH ground state transitions find OH to be extended over wide areas in the Galactic plane (Dawson et al. 2014). The number of absorption detections found in this work is at first glance small relative to the number of cm-continuum sources available in the Galactic plane (e.g., Bihr et al. 2016) and needs to be discussed in terms of the varying sensitivity limit with continuum source strength.

We detect OH absorption mostly against extended Galactic cm-continuum background sources that show a spectral index in agreement with that of free-free emission from H II regions. The lower number of detections of OH in diffuse clouds not associated with H II regions is likely due to the sensitivity limits indicated in Fig. 3. While we do detect OH absorption at a variety of optical depths below $\tau \leq 0.2$ at continuum flux density >1 Jy beam^{-1}, at lower continuum surface brightness the sensitivity is not high enough to detect sources with $\tau \leq 0.05 - 0.1$. As the majority of the continuum sources have a flux density <1 Jy beam^{-1}, we pick up largely absorption at higher optical depths. The increase of the relative number of detections with strength of the continuum source is a further indication that some of the diffuse OH gas (e.g., Dawson et al. 2014) remains undetected for this group of sources.

As diffuse clouds are typically found to have low optical depths (e.g., Liszt & Lucas 1996), we are therefore biased towards higher column densities. As comparison, according to Dickey et al. (1981) using the Nancay telescope at 3′.5 resolution, OH optical depths in diffuse clouds have been found to be approximately 0.05 in a 1 km s^{-1} channel in the 1667 MHz transition. Higher optical depths were found by, e.g., Goss (1968), Yusef-Zadeh et al. (2003) or Stanimirović et al. (2003). OH gas was associated with the Galactic continuum sources, H II regions or supernova remnants (SNR). The detections presented here match more with the latter categories.

4.2. OH as tracer of hydrogen gas

In section 3.2, we compared the OH abundance to the column densities of molecular hydrogen and hydrogen nuclei (hydrogen atoms and molecules). These comparisons are shown in Figs. 8 and 9. OH abundance is found to be decreasing with increasing hydrogen column density. The OH column density is not directly proportional to molecular column density. Therefore, the OH columns densities span a smaller dynamic range than molecular hydrogen. This also indicates that OH traces only specific ranges of molecular cloud column densities.

At any given hydrogen column density, the OH abundance shows variations of a factor of two, which is within the systematic un-

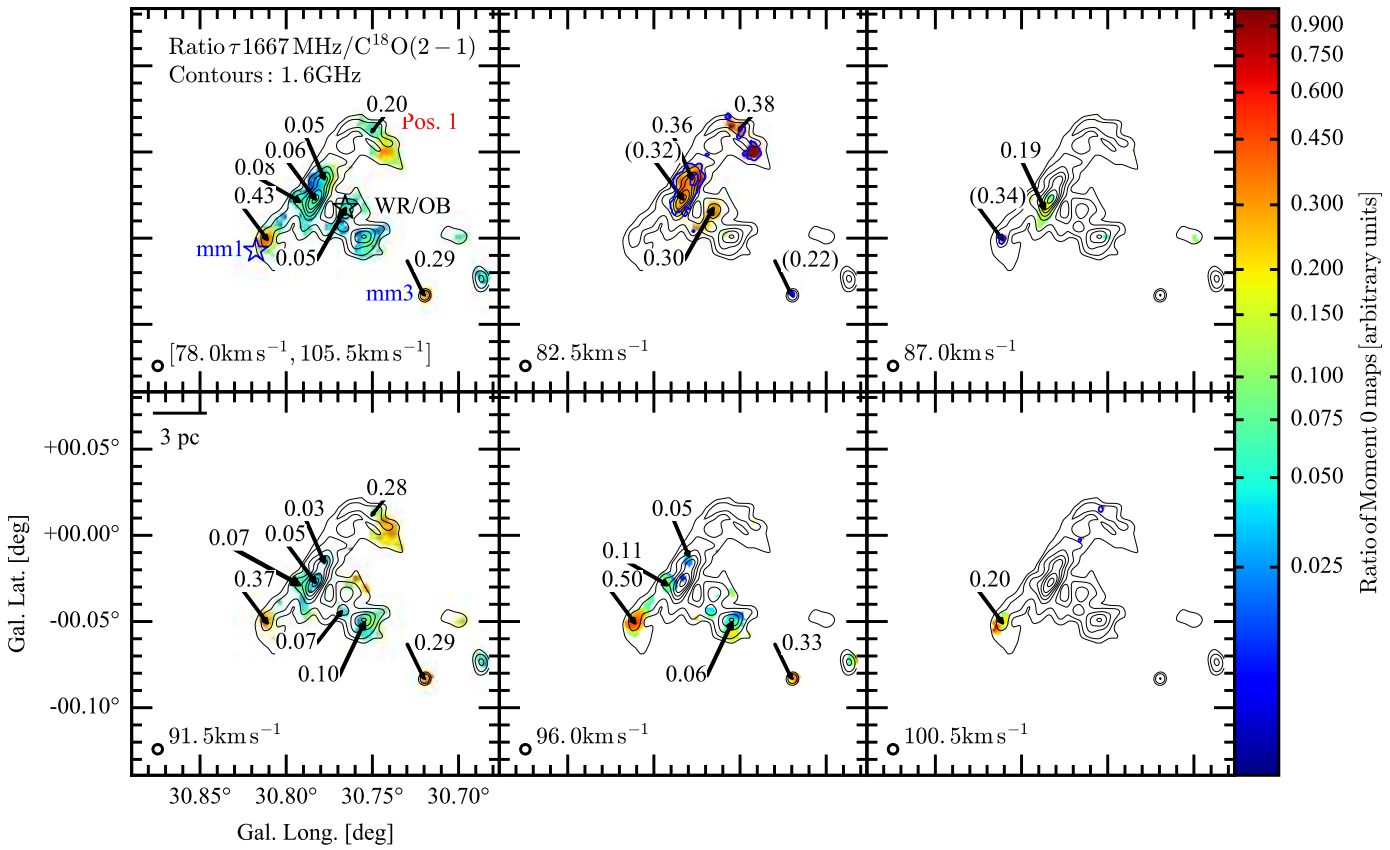

Fig. 11. Ratio of integrated τ(OH 1667 MHz) absorption and $C^{18}O$(2-1) emission in W43. The top-left panel is the same as the rightmost panel in Fig. 10 and is shown for orientation. The other panels show the ratio of τ(OH 1667 MHz) and $C^{18}O$(2-1) at the indicated velocities after binning three channels of 1.5 km s^{-1} width. Overlayed on all panels are contours of 18 cm continuum emission (black, in levels of 0.1, 0.2, 0.4, 0.6, 0.8, 1.0, 1.25, 1.5 and 1.75 Jy beam^{-1}). The 1667 MHz optical depth has been masked at 3-σ detection levels in the original OH absorption data. For pixels with no $C^{18}O$ emission counterpart, 3-σ detection limits have been used, and are indicated by blue contours. The ratio is quoted in brackets for these locations.

certainties. The median value of the OH abundance with respect to N_{H_2} is 1.3×10^{-7}. Within the systematic uncertainties of a factor of 4, this is in agreement with the values reported in the literature, $N_{OH}/N_{H_2} = 1 \times 10^{-7}$ (e.g., Liszt & Lucas 2002).

A constant OH abundance with respect to N_H, as reported by, e.g., Crutcher (1979), can be reproduced - albeit with large scatter - for OH absorption with visual extinctions below $A_V \approx 10 - 20$. A median abundance of $X_{OH}(N_H) \approx 6.1 \times 10^{-8}$ is found for $A_V < 20$. We include atomic hydrogen, as OH may be present in transition regions that contain significant amounts of atomic hydrogen (e.g., Xu et al. 2016; Tang et al. 2017). The H I column density affects the OH abundances at the lowest molecular hydrogen column densities probed, when both are of similar strength. X_{OH} may even be lower in this regime, since the N_{H_I} measurements are lower limits and the N_{H_2} column densities may be underestimated, if the "CO-dark" gas fraction is significant (see Sect. 3.2.5).

Crutcher (1979) finds an abundance of $X_{OH} = 4.0 \times 10^{-8}$, in a range of visual extinction of $A_V = 0.4 - 7$ (see also review by Heiles et al. 1993), which is within the errors of our results. These results are based on studies of nearby molecular clouds (Perseus, Ophiuchus and Taurus), the SNR W44 and line-of-sight observations against extragalactic continuum sources, therefore mainly including observations towards diffuse molecular/translucent clouds (e.g., Snow & McCall 2006) that probably have environments similar to those of clouds that are not associated with H II regions in the sample presented here.

Above visual extinctions of $A_V \approx 10 - 20$, OH abundances are found to be lower than the literature abundance, which is in agreement with theoretical predictions (e.g., Heiles et al. 1993). Oxygen to form OH at these extinctions is likely to be removed from the gas phase by the formation of CO and through the formation of water and its subsequent freeze-out onto grains. Far ultraviolet (FUV) radiation may counteract this removal: Models of photon dominated regions (PDRs) indicate that the local abundance of OH peaks between cloud depths of $A_V \approx 3 - 7$ (e.g., Hollenbach et al. 2009, 2012). According to Hollenbach et al. (2009), the abundance of water in these regions depends on the photodesorption of water ice from dust grains, and OH forms by photodissociation of water in the gas phase. Both water and hydroxyl gas phase abundances thus depend on the flux of the far ultraviolet (FUV) radiation, and decrease once the FUV radiation is efficiently attenuated deeper inside the cloud. As N_{OH} in this work represents a line-of-sight averaged density, OH from more embedded regions in the molecular cloud may contribute less to N_{OH} than ^{13}CO does to N_{H_2}, which may yield a decrease in the line-of-sight averaged OH abundance.

Another possibility for the low OH abundances at high visual extinctions is that the OH excitation temperatures could be higher, approaching the kinetic temperatures in denser and warmer regions of the star forming molecular clouds in our sample. An excitation temperature of, e.g., 20 K would place most of the lowest measured OH abundances at $X_{OH} \sim 1 \times 10^{-7}$ in Fig. 8. As many OH abundances at lower N_{H_2} lie above this value, the trend in

Fig. 8 is likely to persist but to be less steep if higher excitation temperatures at higher N_{H_2} were assumed. This effect is difficult to assess from our data alone, as the excitation temperature cannot be determined independent of the optical depth. Hence, more detailed modelling or targeted observations would be necessary to resolve this ambiguity.

4.3. Comparison with OH column density measurements from other transitions

In this section, we briefly discuss results on the OH column density that had been inferred from observations of other OH transitions. Section 3.3 described the morphologies of the satellite line transitions inside the OH ground state. In three regions, reversal of the 1612 MHz transition from absorption to emission and of the 1720 MHz transition from emission to absorption has been seen. As discussed in Section 3.3, the column density at the transition velocity was inferred using modeling results from van Langevelde et al. (1995). The column densities appear to be by a factor of 3-4 higher than the value inferred from the main lines. As an excitation temperature of 5 K was assumed for the OH ground state transitions, this discrepancy could be remedied by assuming an excitation temperature of $15 - 20$ K, where values up to ∼15 K have been found also in previous works (Colgan et al. 1989).

Additionally, rotational transitions in the far infrared wavelength regime (e.g., Wiesemeyer et al. 2012; Csengeri et al. 2012) or electronic transitions in the optical regime (e.g., Weselak et al. 2010) can be used to study the OH column density. The cross-match with our sample yields a match only for G49.488−0.380 with the source W51e2 in Wiesemeyer et al. (2016). However, the column density at velocities at which OH is detected in this work, is not reported, as the $^2\Pi_{3/2}\, J = 5/2 \leftarrow 3/2$ transitions at 2.5 THz saturate between $50 - 80\,\mathrm{km\,s^{-1}}$.

The OH abundances determined here agree within our systematic uncertainty with the abundances inferred from optical and infrared transitions (Weselak et al. 2010; Wiesemeyer et al. 2016). Figure 13 compares the OH abundances determined here with OH abundances derived from the THz transitions at different lines of sight by Wiesemeyer et al. (2016). Within the sensitivity limits of our survey, for abundances using HF as tracer of H_2, good agreement is seen between both datasets. This is also true for abundances using CH as tracer of H_2, although some points are present between $N_{H_2} \approx 6 - 10 \times 10^{21}\,\mathrm{cm^{-2}}$, which show lower abundance, but are still within uncertainties. Also, for low H_2 column densities, our measurements appear to be sensitivity limited (some measurements from Wiesemeyer et al. (2016) fall below the sensitivity limits indicated in Fig. 13). This comparison affirms the conclusion from Sect. 4.1 that the sample of OH absorption presented here indeed is biased towards high N_{OH}. Conversely, some continuum sources are strong enough to reveal OH absorption in more diffuse molecular cloud regions. Albeit the large systematic uncertainties of X_{OH} here, Fig. 13 shows that the variations in OH abundance at any given N_{H_2} persist when using alternative methods to measure N_{OH} and N_{H_2}, which are possibly less prone to systematics.

4.4. Extended OH absorption towards W43

As W43 is structured in a complicated way, and OH chemistry and excitation may vary strongly in different environments, there may be multiple explanations for variations in the ratios of OH optical depth to $C^{18}O$ and 870 μm emission. For example, there are temperature gradients present in the entire region, which may affect the dust emission.

The peak optical depth of the 1667 MHz transition is typically at $\tau < 1$ in W43. Exceptions are MM1 and MM3, for which optical depth peaks of $\tau_{1667} \sim 1.2$ indicate that the line becomes optically thick (Fig. 12). For MM1, the 1665 MHz transition peaks at $\tau_{1665} \sim 0.6$. Therefore, the ratio of the main lines ($\tau_{1667}/\tau_{1665} \approx 2.0$) is within errors of the expected ratio for LTE excitation of 1.8. For MM3, the ratio of the main lines is closer to unity with $\tau_{1665} \sim 1.0$, indicating that the transitions are not in LTE. As we have no probe of the excitation temperatures, this cannot be further assessed here. We note, however, that deviations from LTE in the OH hyperfine ground state transitions appear to be a common phenomenon (e.g., Li et al. 2018).

In order to minimize the chance of the CO tracers to become optically thick, we choose data from the $C^{18}O$(2-1) transition. Optical thickness even of this transition cannot be ruled out in the entire region, and it will trace regions at higher densities than the ^{13}CO(1-0) used in the rest of the analysis. However, in order to investigate variations on a 20″ scale (0.5 pc) in W43, these data provide information about the molecular gas at matching spatial resolution. As the datasets presented here cannot constrain whether these variations are due to abundance variations or differences in the excitation behavior, we limit the discussion to a qualitative description of the results.

In Figure 11, the enhancement in the OH to $C^{18}O$ ratio around $82.5\,\mathrm{km\,s^{-1}}$ coincides with a peak in radio recombination lines (see velocity distribution of H92α in fig. 6 of Balser et al. 2001 or of cm-RRLs from THOR in fig. 2 of Nguyen-Luong et al. 2017). At this velocity, possibly a photon-dominated, partly ionized region of the cloud is seen, in which models of photon-dominated regions predict the peak of the OH abundance (e.g., Hollenbach et al. 2012).

The OH 1667 MHz to $C^{18}O$ ratios in the center of W43-main at $90-93\,\mathrm{km\,s^{-1}}$ are found to be lower (≤ 0.1; Fig. 11, bottom left panel). This may be due to different physical or chemical conditions of the OH gas, which are difficult to disentangle in a crowded region like W43. Alternatively, this can be a consequence of systematically underestimating the OH optical depth. As described in Sect. 3.2.5, the measured continuum is higher than the true continuum incident on the OH gas, if H II-regions contribute to the continuum emission, which lie between the absorbing cloud and the observer.

This geometry is likely to be present here. The continuum emission at the Wolf-Rayet/OB cluster originates from the H II-region, which emits RRLs between $80-90\,\mathrm{km\,s^{-1}}$. At the T-bar, the RRLs peak between $90-100\,\mathrm{km\,s^{-1}}$, or even at higher velocities close to MM1. Since H II-regions are expanding, gas at lower velocities may be located closer to the observer than higher velocities gas. Absorbing OH gas at $90-100\,\mathrm{km\,s^{-1}}$ would therefore lie between two H II-regions and its measured optical depth can be lower than the true value.

The distribution of absorption in OH and emission in $C^{18}O$ is in agreement with this scenario. In Figure 12, we show spectra of both molecules at different positions. Towards the central Wolf-Rayet cluster, only absorption at $82\,\mathrm{km\,s^{-1}}$ is present, while not detected between $90-95\,\mathrm{km\,s^{-1}}$ in spite of the presence of $C^{18}O$ emission. Towards the center of the T-bar, absorption becomes visible in both velocity ranges. How much and at which lines of sight the optical depth is influenced by this effect, depends on the fractional contribution of each H II-region to the continuum emission. A quantitative assessment of this is beyond the scope of this work.

Close to MM1, the peak of the OH absorption occurs between 96 and 97.5 km s^{-1}. The average velocity of the MM1 complex has been found to be at 98 km s^{-1} (Nguyen Luong et al. 2013) and more resolved observation in HCN(1-0) and SiO(2-1) emission show peaks between 97 and 94 km s^{-1}, respectively, when going from MM1 towards the center of W43-main (Louvet et al. 2016). Louvet et al. indicate low velocity shocks in this region. While this needs to be confirmed, such shocks may produce temperatures that can enhance the OH abundance by activating neutral-neutral chemistry (Neufeld et al. 2002). However, the presence of additional, enhanced UV radiation may be required to produce OH, as neutral-neutral chemistry at high temperatures typically leads to water production (e.g., van Dishoeck et al. 2013). Near MM3 we see emission over a large range of velocities, with a clear peak in optical depth at 93 km s^{-1} in the 1665 MHz line, in agreement with N_2H^+ and SiO peaks at the same velocity (Nguyen Luong et al. 2013).

5. Conclusions

This work gives an overview on the OH absorption against strong continuum background sources as inferred from the THOR survey. This is the first survey-style analysis with the VLA over a significant fraction of the inner Milky Way in the range between $l = 15°$ and $l = 67°$. We detect 59 distinct absorption features against 42 continuum background sources. Most of the absorption is found against Galactic H II regions. We discuss the detection limit in terms of the continuum source strengths.

- Using ^{13}CO(1-0) as tracer for N_{H_2}, we compare the OH abundance (N_{OH}/N_{H_2}) at different N_{H_2}. The OH abundance decreases with increasing hydrogen column density, especially for OH detections in molecular clouds that are associated with H II regions. This can be due to probing cloud regions where the OH in the gas phase is significantly depleted, although varying excitation conditions may provide an alternative explanation. The median abundance is found at $N_{OH}/N_{H_2} \sim 1.3 \times 10^{-7}$, in agreement within errors with previous studies.
- At low column densities, the atomic hydrogen fraction of the gas along the line-of-sight becomes comparable to molecular hydrogen. The OH abundance (N_{OH}/N_H) is found to decrease with increasing total hydrogen nucleus column density for $A_v > 20$, but for lower extinction lines of sight, the data are consistent with a constant abundance having median value $N_{OH}/N_H \sim 6.1 \times 10^{-8}$.
- Extended OH absorption is seen against W43. The OH absorption is compared to ancillary data of 870 μm and C^{18}O emission. At an angular resolution of $20'' \times 20''$, we find variation in the ratios of OH optical depth to emission in 870 μm and C^{18}O, especially towards mm emission sources in the region.

Studies of OH provide a unique insight into the physical conditions of the ISM, particularly the transition between diffuse gas and molecular clouds. This first unbiased interferometric survey is a contribution to the characterization of the variation of OH absorption properties throughout the Galaxy. This work may provide a starting point for theoretical and observational follow-up studies with deeper observations at higher velocity resolution, to expand the sample towards fainter sources with narrower line widths, and in combination with other observational data to resolve the physical conditions of the OH gas, and the molecular content of the diffuse gas surrounding molecular clouds.

Acknowledgements. We thank Joanne R. Dawson for her very useful and insightful comments that helped to improve the clarity of this paper. M.R.R. and H.B. are very grateful for the helpful discussions with C. M. Walmsley at the beginning of the project and for detailed comments on early versions of the manuscript. We thank Morgan Fouesneau for his support on the statistical investigation of the correlation between N_{OH} and N_{H_2}. M.R.R. is a fellow of the International Max Planck Research School for Astronomy and Cosmic Physics (IMPRS) at the University of Heidelberg. M.R.R., H.B., Y.W. and J.S. acknowledge support from the European Research Council under the Horizon 2020 Framework Program via the ERC Consolidator Grant CSF-648505. S.E.R. acknowledges support from the European Union's Horizon 2020 research and innovation programme under the Marie Skłodowska-Curie grant agreement # 706390. F.B. acknowledges funding from the European Union's Horizon 2020 research and innovation programme (grant agreement No 726384 - EMPIRE). J.K. acknowledges funding from the European Union's Horizon 2020 research and innovation programme under grant agreement No 639459 (PROMISE). R.S.K., S.C.O.G., M.R.R. and H.B. acknowledge support from the Deutsche Forschungsgemeinschaft in the Collaborative Research Center (SFB 881) "The Milky Way System" (subprojects B1, B2, and B8). R.S.K. and S.C.O.G. acknowledge support from the Deutsche Forschungsgemeinschaft in the Priority Program SPP 1573 "Physics of the Interstellar Medium" (grant numbers KL 1358/18.1, KL 1358/19.2, GL 668/2-1). R.S.K. furthermore thanks the European Research Council for funding in the ERC Advanced Grant STARLIGHT (project number 339177). This work was carried out in part at the Jet Propulsion Laboratory, which is operated for NASA by the California Institute of Technology. N.R. acknowledges support from the Infosys Foundation through the Infosys Young Investigator grant. N.S. acknowledges support by the French ANR and the German DFG through the project "GENESIS" (ANR-16-CE92-0035-01/DFG1591/2-1). RJS gratefully acknowledges support through an STFC Ernest Rutherford Fellowship. This research made use of Astropy and affiliated packages, a community-developed core Python package for Astronomy (Astropy Collaboration et al. 2013) and the VizieR catalogue access tool, CDS, Strasbourg, France.

References

Allen, R. J., Hogg, D. E., & Engelke, P. D. 2015, AJ, 149, 123
Anderson, L. D., Bania, T. M., Balser, D. S., et al. 2014, ApJS, 212, 1
Anderson, L. D., Bania, T. M., Jackson, J. M., et al. 2009, ApJS, 181, 255
Argon, A. L., Reid, M. J., & Menten, K. M. 2000, ApJS, 129, 159
Astropy Collaboration, Robitaille, T. P., Tollerud, E. J., et al. 2013, A&A, 558, A33
Bally, J., Anderson, L. D., Battersby, C., et al. 2010, A&A, 518, L90
Balser, D. S., Goss, W. M., & De Pree, C. G. 2001, AJ, 121, 371
Beuther, H., Bihr, S., Rugel, M., et al. 2016, A&A, 595, A32
Beuther, H., Tackenberg, J., Linz, H., et al. 2012, A&A, 538, A11
Bialy, S., Bihr, S., Beuther, H., Henning, T., & Sternberg, A. 2017, ApJ, 835, 126
Bihr, S., Beuther, H., Ott, J., et al. 2015, A&A, 580, A112
Bihr, S., Johnston, K. G., Beuther, H., et al. 2016, A&A, 588, A97
Blaauw, A., Gum, C. S., Pawsey, J. L., & Westerhout, G. 1960, MNRAS, 121, 123
Blum, R. D., Damineli, A., & Conti, P. S. 1999, AJ, 117, 1392
Bohlin, R. C., Savage, B. D., & Drake, J. F. 1978, ApJ, 224, 132
Bolatto, A. D., Wolfire, M., & Leroy, A. K. 2013, ARA&A, 51, 207
Bourke, T. L., Myers, P. C., Robinson, G., & Hyland, A. R. 2001, ApJ, 554, 916
Brooks, K. J. & Whiteoak, J. B. 2001, MNRAS, 320, 465
Carlhoff, P., Nguyen Luong, Q., Schilke, P., et al. 2013, A&A, 560, A24
Cesaroni, R. & Walmsley, C. M. 1991, A&A, 241, 537
Colgan, S. W. J., Salpeter, E. E., & Terzian, Y. 1989, ApJ, 336, 231
Contreras, Y., Schuller, F., Urquhart, J. S., et al. 2013, A&A, 549, A45
Crutcher, R. M. 1977, ApJ, 216, 308
Crutcher, R. M. 1979, ApJ, 234, 881
Csengeri, T., Menten, K. M., Wyrowski, F., et al. 2012, A&A, 542, L8
Dawson, J. R., Walsh, A. J., Jones, P. A., et al. 2014, MNRAS, 439, 1596
Dickey, J. M., Crovisier, J., & Kazes, I. 1981, A&A, 98, 271
Dobbs, C. L., Krumholz, M. R., Ballesteros-Paredes, J., et al. 2014, in Protostars and Planets VI, ed. H. Beuther, R. S. Klessen, C. P. Dullemond, & T. Henning, 3–26
Ebisawa, Y., Inokuma, H., Sakai, N., et al. 2015, ApJ, 815, 13
Elitzur, M. 1992, Astrophysics and Space Science Library, Vol. 170, Astronomical masers (Dordrecht: Kluwer Academic Publishers)
Frayer, D. T., Seaquist, E. R., & Frail, D. A. 1998, AJ, 115, 559
Frerking, M. A., Langer, W. D., & Wilson, R. W. 1982, ApJ, 262, 590
Ginsburg, A., Bressert, E., Bally, J., & Battersby, C. 2012, ApJ, 758, L29
Goodman, A. A., Alves, J., Beaumont, C. N., et al. 2014, ApJ, 797, 53

Goss, W. M. 1968, ApJS, 15, 131
Grenier, I. A., Casandjian, J.-M., & Terrier, R. 2005, Science, 307, 1292
Guelin, M. 1985, in Molecular astrophysics: State of the art and future directions, ed. G. H. F. Diercksen, W. F. Huebner, & P. W. Langhoff, Proceedings of the Advanced Research Workshop, Bad Windsheim, West Germany, July 8-14, 1984 (A86-39726 18-90) (Dordrecht: D. Reidel Publishing), 23–43
Guibert, J., Rieu, N. Q., & Elitzur, M. 1978, A&A, 66, 395
Hales, C. A., Murphy, T., Curran, J. R., et al. 2012, MNRAS, 425, 979
Heiles, C., Goodman, A. A., McKee, C. F., & Zweibel, E. G. 1993, in Protostars and Planets III, ed. E. H. Levy & J. I. Lunine, 279–326
Heyer, M. & Dame, T. M. 2015, ARA&A, 53, 583
Hollenbach, D., Kaufman, M. J., Bergin, E. A., & Melnick, G. J. 2009, ApJ, 690, 1497
Hollenbach, D., Kaufman, M. J., Neufeld, D., Wolfire, M., & Goicoechea, J. R. 2012, ApJ, 754, 105
Jackson, J. M., Rathborne, J. M., Shah, R. Y., et al. 2006, ApJS, 163, 145
Klessen, R. S. & Glover, S. C. O. 2016, Saas-Fee Advanced Course, Vol. 43, Physical Processes in the Interstellar Medium, ed. Y. Revaz, P. Jablonka, R. Teyssier, & L. Mayer (Springer Berlin Heidelberg), 85–249
Langer, W. D. & Graedel, T. E. 1989, ApJS, 69, 241
Lester, D. F., Dinerstein, H. L., Werner, M. W., et al. 1985, ApJ, 296, 565
Li, D. & Goldsmith, P. F. 2003, ApJ, 585, 823
Li, D., Tang, N., Nguyen, H., et al. 2018, ArXiv e-prints [arXiv:1801.04373]
Liszt, H. & Lucas, R. 1996, A&A, 314, 917
Liszt, H. & Lucas, R. 1999, in Astronomical Society of the Pacific Conference Series, Vol. 156, Highly Redshifted Radio Lines, ed. C. L. Carilli, S. J. E. Radford, K. M. Menten, & G. I. Langston, 188
Liszt, H. & Lucas, R. 2002, A&A, 391, 693
Liszt, H. S. 1995, AJ, 109, 1204
Louvet, F., Motte, F., Gusdorf, A., et al. 2016, A&A, 595, A122
McKee, C. F. & Ostriker, E. C. 2007, ARA&A, 45, 565
Milam, S. N., Savage, C., Brewster, M. A., Ziurys, L. M., & Wyckoff, S. 2005, ApJ, 634, 1126
Miville-Deschênes, M.-A., Murray, N., & Lee, E. J. 2017, ApJ, 834, 57
Motte, F., Nguyen Luong, Q., Schneider, N., et al. 2014, A&A, 571, A32
Motte, F., Schilke, P., & Lis, D. C. 2003, ApJ, 582, 277
Mottram, J. C. & Brunt, C. M. 2010, in Astronomical Society of the Pacific Conference Series, Vol. 438, The Dynamic Interstellar Medium: A Celebration of the Canadian Galactic Plane Survey, ed. R. Kothes, T. L. Landecker, & A. G. Willis, 98
Neufeld, D. A., Kaufman, M. J., Goldsmith, P. F., Hollenbach, D. J., & Plume, R. 2002, ApJ, 580, 278
Nguyen-Luong, Q., Anderson, L. D., Motte, F., et al. 2017, ApJ, 844, L25
Nguyen Luong, Q., Motte, F., Carlhoff, P., et al. 2013, ApJ, 775, 88
Nguyen Luong, Q., Motte, F., Schuller, F., et al. 2011, A&A, 529, A41
Nishimura, A., Tokuda, K., Kimura, K., et al. 2015, ApJS, 216, 18
Offer, A., van Hemert, M., & van Dishoeck, E. . 1994, J. Che. Phys., 100
Phillips, T. G., Knapp, G. R., Wannier, P. G., et al. 1981, ApJ, 245, 512
Pihlström, Y. M., Fish, V. L., Sjouwerman, L. O., et al. 2008, ApJ, 676, 371
Pineda, J. E., Caselli, P., & Goodman, A. A. 2008, ApJ, 679, 481
Pineda, J. L., Goldsmith, P. F., Chapman, N., et al. 2010, ApJ, 721, 686
Pineda, J. L., Langer, W. D., Velusamy, T., & Goldsmith, P. F. 2013, A&A, 554, A103
Planck Collaboration, Ade, P. A. R., Aghanim, N., et al. 2011, A&A, 536, A19
Ragan, S. E., Henning, T., Tackenberg, J., et al. 2014, A&A, 568, A73
Reid, M. J., Menten, K. M., Brunthaler, A., et al. 2014, ApJ, 783, 130
Reifenstein, E. C., Wilson, T. L., Burke, B. F., Mezger, P. G., & Altenhoff, W. J. 1970, A&A, 4, 357
Schöier, F. L., van der Tak, F. F. S., van Dishoeck, E. F., & Black, J. H. 2005, A&A, 432, 369
Schuller, F., Menten, K. M., Contreras, Y., et al. 2009, A&A, 504, 415
Smith, L. F., Biermann, P., & Mezger, P. G. 1978, A&A, 66, 65
Smith, R. J., Glover, S. C. O., Clark, P. C., Klessen, R. S., & Springel, V. 2014, MNRAS, 441, 1628
Snow, T. P. & McCall, B. J. 2006, ARA&A, 44, 367
Stanimirović, S., Weisberg, J. M., Dickey, J. M., et al. 2003, ApJ, 592, 953
Stil, J. M., Taylor, A. R., Dickey, J. M., et al. 2006, AJ, 132, 1158
Szűcs, L., Glover, S. C. O., & Klessen, R. S. 2016, MNRAS, 460, 82
Tang, N., Li, D., Heiles, C., et al. 2017, ApJ, 839, 8
Turner, B. E. 1966, Nature, 212, 184
Turner, B. E. 1973, ApJ, 186, 357
Turner, B. E. 1979, A&AS, 37, 1
Turner, B. E. & Heiles, C. 1971, ApJ, 170, 453
Urquhart, J. S., Csengeri, T., Wyrowski, F., et al. 2014, A&A, 568, A41
Urquhart, J. S., Thompson, M. A., Moore, T. J. T., et al. 2013, MNRAS, 435, 400
van Dishoeck, E. F., Herbst, E., & Neufeld, D. A. 2013, Chemical Reviews, 113, 9043
van Langevelde, H. J., van Dishoeck, E. F., Sevenster, M. N., & Israel, F. P. 1995, ApJ, 448, L123
Walsh, A. J., Beuther, H., Bihr, S., et al. 2016, MNRAS, 455, 3494
Wannier, P. G., Andersson, B.-G., Federman, S. R., et al. 1993, ApJ, 407, 163
Weinreb, S., Barrett, A. H., Meeks, M. L., & Henry, J. C. 1963, Nature, 200, 829
Weselak, T., Galazutdinov, G. A., Beletsky, Y., & Krełowski, J. 2010, MNRAS, 402, 1991
Wiesemeyer, H., Güsten, R., Heyminck, S., et al. 2016, A&A, 585, A76
Wiesemeyer, H., Güsten, R., Heyminck, S., et al. 2012, A&A, 542, L7
Wilson, T. L., Rohlfs, K., & Hüttemeister, S. 2009, Tools of Radio Astronomy (Springer-Verlag)
Xu, D., Li, D., Yue, N., & Goldsmith, P. F. 2016, ApJ, 819, 22
Yusef-Zadeh, F., Wardle, M., & Roberts, D. A. 2003, ApJ, 583, 267
Zhang, B., Moscadelli, L., Sato, M., et al. 2014, ApJ, 781, 89

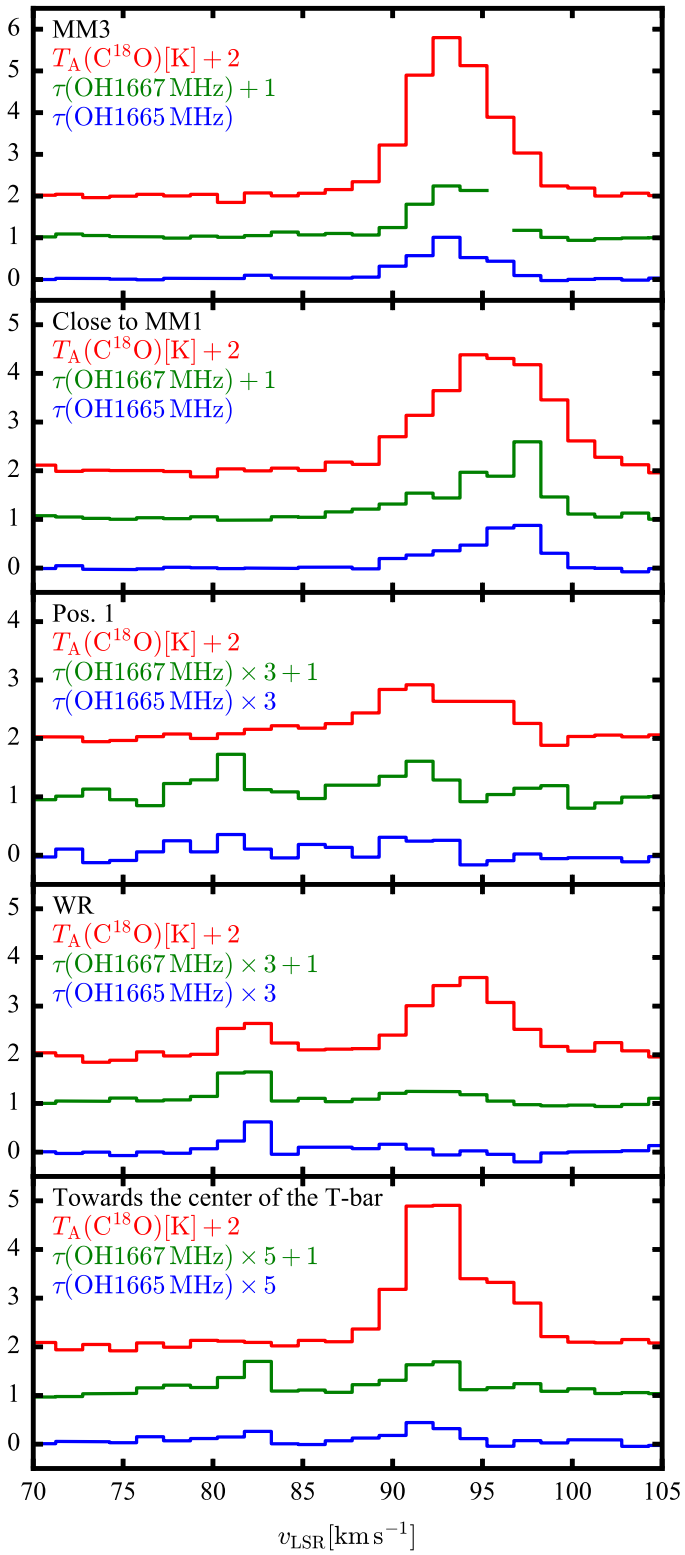

Fig. 12. Spectra of τ_{OH} in the 1665 and 1667 MHz lines, as well as of emission in $C^{18}O(2–1)$ line. The spectra are extracted towards positions MM1, MM3[6], WR and "Pos. 1" as indicated in Figs. 10 and 11, as well as towards the central part of the T-bar. Towards MM3, the channel at 96 km s^{-1} of the OH 1667 MHz absorption is masked because of sidelobes of close-by maser emission.

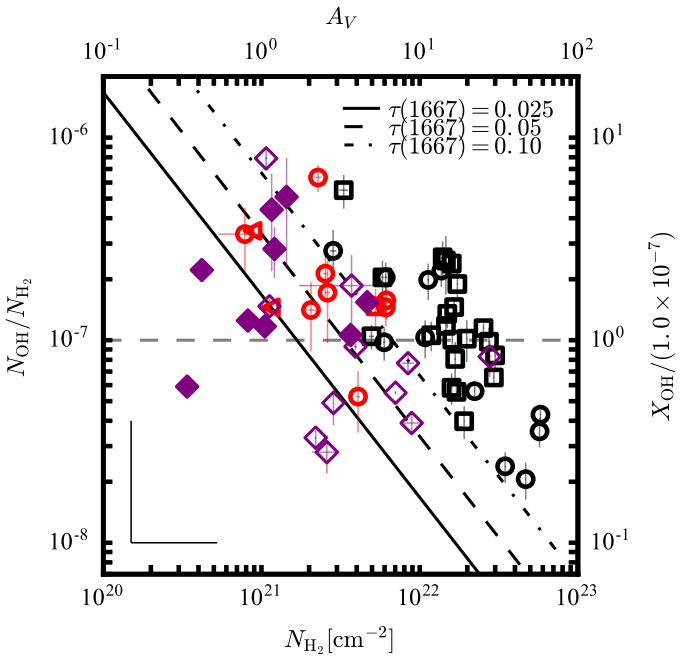

Fig. 13. Comparison of the OH molecular abundances from this work to abundances measured in Wiesemeyer et al. (2016). Data, symbols and systematic uncertainties as in Fig. 8. Measurements from table 4 of Wiesemeyer et al. (2016) are overplotted as purple diamonds. Filled diamonds use HF as proxy for the H_2 column density. Empty diamonds use CH. If both HF and CH measurements are available, OH measurements are drawn twice. Black diagonal lines indicate sensitivity limits of X_{OH} for typical 4-σ limits on optical depth in the OH main lines and assuming a line width of 2.5 km s^{-1} (The detection limits of τ = 0.025, 0.05 and 0.1 are acchieved for continuum sources stronger than F_{cont} = 2.10, 1.05 and 0.53 Jy beam^{-1}, respectively).

Table 3. Derived quantities from OH 1665/1667 MHz and H I absorption and ^{13}CO(1-0) emission.

Name	v	$N_{\rm OH\,1665}/T_{\rm ex}$	$N_{\rm OH\,1667}/T_{\rm ex}$	v	$N_{^{13}\rm CO}$	$N_{\rm H_2}$	$N_{\rm H\,I}$	Notes	$X_{\rm OH}(N_{\rm H})$	$X_{\rm OH}(N_{\rm H_2})$
	$\left[\frac{\rm km}{\rm s}\right]$	$\left[\times\frac{10^{14}}{\rm cm^2 K}\right]$	$\left[\times\frac{10^{14}}{\rm cm^2 K}\right]$	$\left[\frac{\rm km}{\rm s}\right]$	$\left[\times\frac{10^{16}}{\rm cm^2}\right]$	$\left[\times\frac{10^{21}}{\rm cm^2}\right]$	$\left[\times\frac{10^{21}}{\rm cm^2}\right]$		$[\times10^{-7}]$	$[\times10^{-7}]$
G14.490+0.021	23.1	<5.4 ± 2.4[a]	–	–	–	–	>1.3	2(OH)	–	–
G14.996−0.738	21.8	1.5 ± 0.4	–	–	–	–	>6.3	1	–	–
G15.033−0.679	12.9	0.8 ± 0.2	–	–	–	–	>4.6	1	–	–
G18.148−0.283	56.4	3.2 ± 0.4	–	55.5	4.2	16.1	>3.0	1665	>0.5	1.0
G18.303−0.390	27.2	–[b]	–	–	–	–	–	3(OH)	–	–
	32.2	1.9 ± 0.2	–	33.0	4.5	17.1	>2.5	1665	>0.3	0.6
	36.2	–[b]	–	–	–	–	–	3(OH)	–	–
G19.075−0.288	64.6	5.4 ± 0.9	–	65.1	7.2	27.4	>4.1	1665	>0.5	1.0
G21.347−0.629	56.1	1.9 ± 0.3	–	56.2	2.8	10.7	>3.3	4(CO)	–	–
G21.874+0.007	21.8	4.0 ± 0.6	–	22.3	3.9	14.9	>3.5	1665	>0.6	1.3
G23.956+0.150	80.0	1.5 ± 0.3	–	79.6	5.0	19.1	>3.5	1665	>0.2	0.4
G25.396+0.033	−12.1	3.2 ± 0.6	–	–	–	–	>1.3	1	–	–
G25.397−0.141	67.1	1.0 ± 0.1	–	66.5	1.3	5.0	>5.1	1665	>0.3	1.0
	94.5	3.9 ± 0.3	–	96.3	7.7	29.4	>4.2	1665	>0.3	0.7
G26.609−0.212	−33.2	3.1 ± 1.3	–	–	–	–	>1.5	1	–	–
G27.563+0.084	86.0	7.2 ± 2.3	–	85.8	3.9	14.6	>2.0	1665	>1.2	2.5
G28.806+0.174	79.8	1.5 ± 0.3	–	80.6	1.4	5.3	>2.8	1665	>0.6	1.5
	103.5	1.5 ± 0.6	–	104.8	5.4	20.4	>2.5	4(CO)	–	–
G29.935−0.053	7.0	<0.6 ± 0.2	0.2 ± 0.1	–	<0.3	<1.1	>1.6	1667	>0.4	1.5
	50.6	<0.6 ± 0.2	0.3 ± 0.1	49.9	1.1	4.1	>2.3	1667	>0.2	0.5
	68.0	<0.6 ± 0.2	0.4 ± 0.2	68.1	0.5	2.1	>4.2	1667	>0.3	1.4
	98.9	1.9 ± 0.5	1.4 ± 0.3	99.4	12.3	46.8	>4.9	1667	>0.1	0.2
G29.957−0.018	8.0	0.3 ± 0.1	0.4 ± 0.1	7.4	0.2	0.8	>2.2	1667	>0.7	3.3
	99.8	–[c]	0.4 ± 0.1	98.0	13.1	49.9	>4.5	4(CO)	–	–
G30.535+0.021	43.7	–[c]	–[b]	–	–	–	–	2(OH)	–	–
	49.4	1.1 ± 0.5	1.3 ± 0.4	47.7	5.5	20.8	>4.0	2(OH)	–	–
	91.6	2.7 ± 0.5	1.7 ± 0.4	91.9	2.8	10.8	>3.3	1667	>0.4	1.0
G30.720−0.083	93.6	–[c]	–[c]	94.0	9.5	36.1	>4.4	7	–	–
G30.783−0.028	77.9	–	–[b]	–	–	–	–	3(OH)	–	–
	81.9	0.8 ± 0.1	0.9 ± 0.2	81.9	1.6	6.0	>3.4	1667	>0.4	1.0
	87.1	–[b]	–	–	–	–	–	3(OH)	–	–
	92.1	1.5 ± 0.3	1.2 ± 0.2	93.3	9.1	34.7	>7.2	1667	>0.1	0.2
	98.6	–[b]	–[b]	104.9	–	–	3(OH)	–	–	
G30.854+0.151	95.4	5.4 ± 0.9	4.5 ± 0.8	95.5	3.6	13.7	>1.3	1667	>1.1	2.2
G31.242−0.110	19.6	–[c]	1.9 ± 0.3	20.8	1.6	6.1	>2.5	1667	>0.8	2.0
	79.2	2.3 ± 0.4	1.4 ± 0.3	78.8	1.6	6.2	>2.1	1667	>0.7	1.6
	83.7	<1.1 ± 0.3	0.7 ± 0.3	84.0	0.7	2.6	>1.3	1667	>0.7	1.7
G31.388−0.383	18.1	0.7 ± 0.2	0.5 ± 0.1	–	<0.2	<0.9	>3.2	1667	>0.6	3.5
G32.151+0.132	93.8	4.8 ± 0.6	–	94.4	4.3	16.5	>2.4	1665	>0.7	1.5
G32.272−0.226	22.6	3.6 ± 0.6	–	22.4	0.9	3.3	>2.1	1665	>2.1	5.5
G32.798+0.190	12.8	5.8 ± 0.3	–	15.1	6.7	25.3	>8.1	1665	>0.5	1.1
G32.928+0.607	−33.9	2.5 ± 1.1[a]	–	–	–	–	>2.8	1	–	–
G33.915+0.110	95.3	0.6 ± 0.2[a]	–	–	<0.3	<1.1	>0.6	2(OH)	–	–
	101.5	1.1 ± 0.2[a]	–	–	<0.3	<1.1	>1.5	2(OH)	–	–
	106.3	1.9 ± 0.3	–	107.5	4.2	15.9	>1.9	1665	>0.3	0.6
G34.132+0.471	33.8	2.4 ± 0.5	–	35.1	1.5	5.8	>3.4	1665	>0.8	2.0
G35.467+0.139	77.0	3.4 ± 0.8	–	77.4	3.9	14.6	>1.3	1665	>0.6	1.2
G37.764−0.215	63.4	6.6 ± 0.9	–	61.5	4.6	17.3	>5.7	1665	>0.8	1.9
G37.874−0.399	61.0	7.6 ± 0.9	–	61.4	4.2	15.9	>8.8	1665	>0.9	2.4
G38.876+0.308	−16.3	4.1 ± 0.7	4.0 ± 0.6	–	–	–	>1.7	1	–	–
G39.565−0.040	23.2	2.6 ± 0.4	2.2 ± 0.3	23.4	0.6	2.3	>3.6	1667	>1.8	6.4
G39.883−0.346	56.9	4.9 ± 1.0	3.4 ± 0.7	58.7	3.0	11.3	>2.9	1667	>0.9	2.0
G41.741+0.097	14.2	1.9 ± 0.7	1.2 ± 0.3	13.4	0.7	2.8	>1.2	1667	>1.1	2.8
G42.027−0.604	65.1	<1.3 ± 0.4	1.3 ± 0.3	65.5	1.6	6.1	>3.1	1667	>0.6	1.5
G45.454+0.060	56.0	–	–[b]	–	–	–	–	3(OH)	–	–
	59.4	–[c]	1.9 ± 0.2	58.9	5.9	22.2	>5.5	1667	>0.2	0.6
	64.9	–	–[c]	–	–	–	–	3(OH)	–	–
G49.206−0.342	65.3	7.2 ± 1.4	–	65.7	3.7	14.0	>6.9	1665	>1.0	2.6
G49.369−0.302	50.9	5.0 ± 0.7	–	51.1	7.9	30.0	>6.2	1665	>0.4	0.8
	62.9	2.5 ± 0.4	–	61.1	3.1	11.8	>5.4	1665	>0.4	1.1
G49.459−0.353	62.0	2.7 ± 0.6	–	61.1	4.4	16.8	>5.5	1665	>0.3	0.8
	68.6	4.0 ± 0.9	–	68.6	5.2	19.8	>3.9	1665	>0.5	1.0
G49.488−0.380	65.9	1.9 ± 0.4	–	67.8	5.8	22.0	>4.7	4	–	–
G52.753+0.334	12.1	<1.4± 0.4[a]	0.7 ± 0.3	–	0.9	3.5	>2.1	7	–	–
	45.2	<1.3± 0.3[a]	0.8 ± 0.2	44.5	0.7	2.5	>1.4	1667	>0.8	2.1
G60.882−0.132	22.3	2.8 ± 0.7	3.0 ± 0.5	22.4	15.1	57.2	>2.1	1667	>0.2	0.4
G61.475+0.092	5.9	<0.12 ±0.03	0.1 ± 0.0[a]	6.6	0.1	0.2	>1.6	2(OH)	–	–
	21.1	4.9 ± 0.2	3.7 ± 0.2	21.6	15.3	58.0	>4.0	1667	>0.2	0.4

Notes. $N_{\rm OH\,1665\,MHz}/T_{\rm ex}$, $N_{\rm OH\,1667\,MHz}/T_{\rm ex}$ and $N_{\rm H\,I}$ are determined from the integrated optical depth (Table 2; see text for the conversions used). The velocity is the mean of the center velocities of the OH 1665 MHz and OH 1667 MHz absorption. The column density of molecular hydrogen, $N_{\rm H_2}$, is derived from ^{13}CO emission (for assumptions and conversions see text). $X_{\rm OH}(N_{\rm H})$ is defined as $N_{\rm OH}/N_{\rm H}$, with $N_{\rm H} = N_{\rm H\,I} + 2N_{\rm H_2}$, while $X_{\rm OH}(N_{\rm H_2})$ is the ratio $N_{\rm OH}/N_{\rm H_2}$. Notes and footnotes are as in Table 2.

Table 4. Conjugate inversion and anti-inversion of satellite lines

Name	1612	1720	v [km/s]
G18.303−0.390	E	A	31.5
G19.075−0.288	A	E	58.5
	R	R	67.5
	E	A	70.0
G25.396+0.033	E	A	−12.0
G25.397−0.141	E	A	96.0
G29.935−0.053	A	–	97.0
	R	–	98.5
	E	A	100.0
G29.957−0.018	E	A	100.5
G30.535+0.021	E	A	45.0
G30.535+0.021	A	E	92.0
G30.720−0.083	E	A	93.0
G30.783−0.028	E	A	82.0
G32.151+0.132	E	A	94.5
G32.798+0.190	A	E	12.0
	R	R	14.0
	E	A	18.0
G32.798+0.190	A	E	90.0
G33.915+0.110	E	A	105.0
G37.764−0.215	A	–	62.5
	R	R	65.0
	–	A	67.5
G37.874−0.399	E	A	58.5
G38.876+0.308	E	A	−16.5
G39.883−0.346	E	A	57.0
G41.741+0.097	E	A	14.0
G49.206−0.342	A	–	65.0
	R	–	66.0
	E	A	68.0
G49.369−0.302	A	–	49.0
	R	–	49.5
	E	A	53.0
G49.369−0.302	A	E	62.5
	R	R	63.5
	E	A	65.0
G49.459−0.353	A	E	69.0
G60.882−0.132	E	A	22.5

Notes. Columns 2 and 3 indicate conjugate absorption (*A*) and emission (*E*) of the OH 1612 MHz and OH 1720 MHz transitions. The corresponding velocity is given in column 4. In some cases, 1612 MHz absorption and 1720 MHz emission transform into 1612 MHz emission and 1720 MHz absorption at higher velocities. For this kind of profile we give three entries: the central velocities of absorption and emission as well as the velocity, at which the reversal (R) of the line profile occurs. This is defined here as the velocity at which the satellite lines are equal. Components of the reversal profile that are not detected significantly are indicated by a horizontal dash.

Appendix A: Detection of OH main line absorption – notes on individual sources

- G23.956+0.150, +81.0 km s^{-1}: One velocity channel is above 4-σ and two above 3-σ. There is a corresponding ^{13}CO(1-0) counterpart.
- G26.609−0.212, −33.0 km s^{-1}: One velocity channel is detected at 4-σ, another at 3-σ. The ^{13}CO(1-0) data do not cover these velocities.
- G28.806+0.174, +79.5 km s^{-1}: One velocity channel is detected at 4-σ, a ^{13}CO(1-0) counterpart exists that matches well in velocity.
- G28.806+0.174, +103.0 km s^{-1}: One velocity channel is detected at 4-σ, a ^{13}CO(1-0) counterpart exists that contains blended components.
- G29.935−0.053, +51.0 km s^{-1}: This object is detected at 4-σ. Also, a ^{13}CO(1-0) counterpart exists.
- G29.935−0.053, +7.5 km s^{-1}: This object is detected in one velocity channel at 3-σ and in one at 5-σ after smoothing to 46″ resolution. The detection is not picked up in the 1665 MHz transition. There is no ^{13}CO(1-0) emission at this velocity.
- G30.535+0.021, +45.0 km s^{-1}: This feature shows one velocity channel at 4-σ and three at 3-σ in the 1667 MHz transition. We compare this feature to ^{13}CO(1-0), after smoothing to 46″. The feature peaks at 43.5 km s^{-1}. In comparison, the ^{13}CO(1-0) shows two distinct peaks at 40.3 and 47.3 km s^{-1}. Interestingly, the trough between both features occurs at the position of the OH peak. The trough could be a sign of CO self-absorption, i.e. the absorption by cold CO gas of the line emission from a warmer background source (e.g., Phillips et al. 1981). A possible heating source of the background CO gas could be the H II-region G30.539−00.024, which emits RRLs at 46 km s^{-1} (Table 1; Anderson et al. 2014).
- G30.535+0.021, +92.0 km s^{-1}: This feature shows one velocity channel at 4-σ and three at 3-σ in the 1667 MHz transition. The feature peaks at 92 km s^{-1} and we compare it to ^{13}CO(1-0) emission, after smoothing to 46″. The ^{13}CO(1-0) seems to have blended components. In the 1665 MHz transition the feature is weakly detected (at 3-σ). However, it has a different shape to the 1667 MHz transition – most likely due to its weak detection – and so we do not include it for fitting the line width, but instead merely use it for the column density comparison.
- G32.272−0.226, +22.5 km s^{-1}: In this feature, three velocity channels are detected at 4-σ. There is a corresponding feature in ^{13}CO(1-0) that spreads over a similar velocity range but the line profile is not centrally peaked. This is confirmed by investigating the ^{13}CO(1-0) emission around this position, with the strongest individual peak being located at 22.7 km s^{-1}. The noise was checked a few arc minutes away from the emission and did not show any anomalies in this velocity range.
- G32.928+0.607, −34.5 km s^{-1}: This feature contains one pixel at 3-σ in the 1665 MHz transition. No ^{13}CO(1-0) data are available for comparison at this velocity.
- G35.467+0.139, +78.0 km s^{-1}: This feature consists of two velocity channels close to a signal-to-noise ratio of 4-σ. There exists ^{13}CO(1-0) emission that peaks at a similar velocity.
- G60.882−0.132, +22.5 km s^{-1}: OH absorption in the 1667 MHz transition is detected, with one velocity channel at 3-σ, 4-σ and 5-σ, respectively. In the 1665 MHz transition, one velocity bin is detected at 5-σ . Also, we find a ^{13}CO(1-0) counterpart at similar velocity.

Appendix B: Estimation of the correlation between $N_{\rm OH}$ and $N_{\rm H_2}$

We provide additional information on the estimation of the correlation between $N_{\rm OH}$ and $N_{\rm H_2}$ from Sect. 3.2.6. For numerical stability, we center all data on the mean of the measured column densities, $\overline{N_{\rm OH}}$ and $\overline{N_{\rm H_2}}$. We perform the linear regression on $\log(N_{\rm OH}/\overline{N_{\rm OH}}) = m \times \log(N_{\rm H_2}/\overline{N_{\rm H_2}}) + t_{\rm centered}$. The parameter t from Sect. 3.2.6 relates to the sampled $t_{\rm centered}$ as $t = t_{\rm centered} + \log(\overline{N_{\rm OH}}) - m \times \log(\overline{N_{\rm H_2}})$. The median, 16%-, and 84%-percentiles are $m = 0.32^{+0.13}_{-0.13}$, $t_{\rm centered} = -0.05^{+0.06}_{-0.06}$ and $t = 8.04^{+2.77}_{-2.88}$. Fig. B.1 shows the histogram of the marginalized distributions of m and $t_{\rm centered}$.

Appendix C: Individual sources – transitions of the OH ground state

This appendix shows the spectra of the OH ground state transitions.

Appendix D: Individual sources – OH optical depth, ^{13}CO(1-0) emission and H I absorption

The appendix shows the OH and H I optical depth profiles for each source, as well as the ^{13}CO(1-0) emission.

Appendix E: OH absorption towards W43

Moment zero map of the optical depth of the 1667 MHz transition for different velocity intervals towards W43.

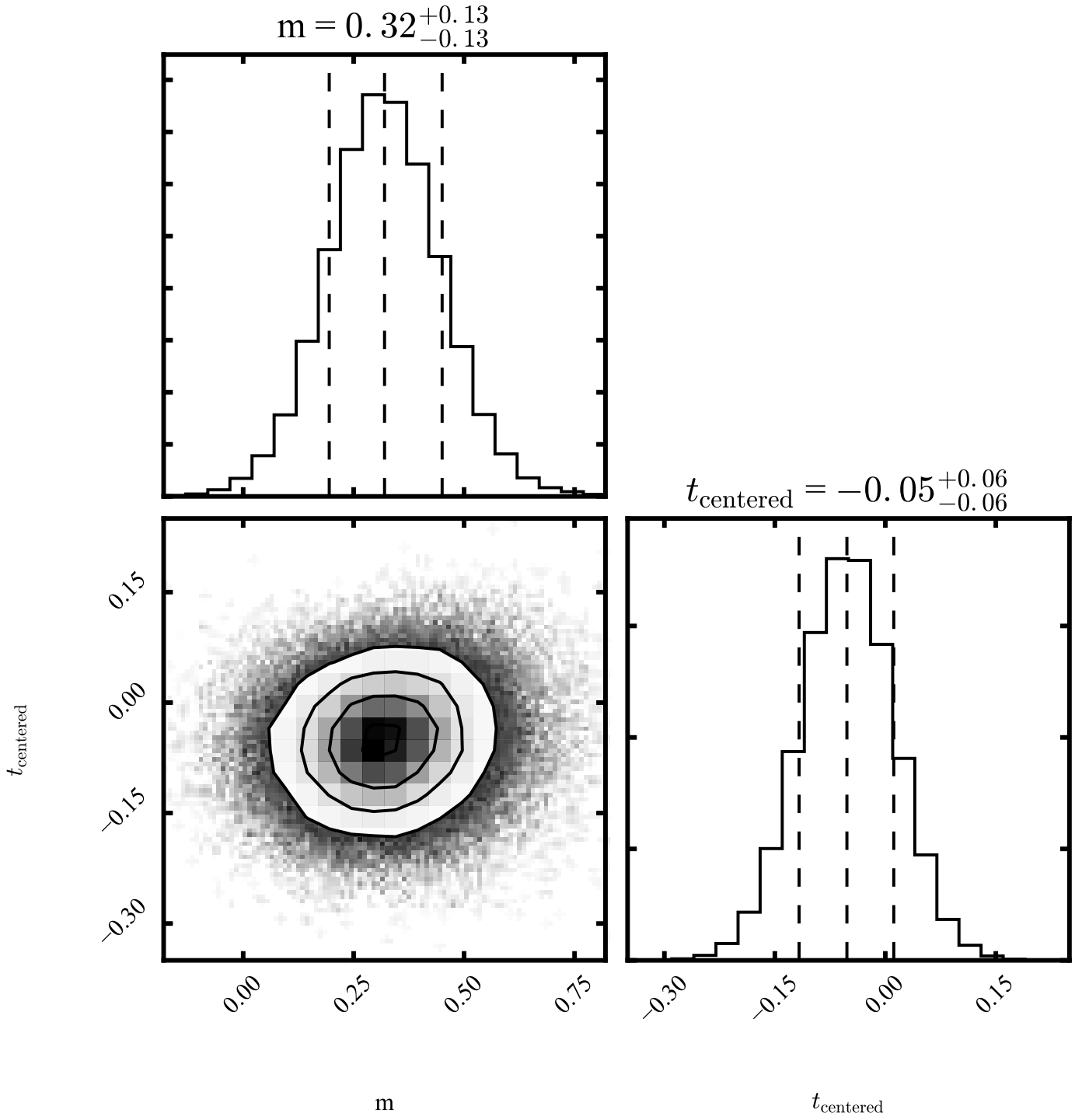

Fig. B.1. Marginalized distributions of m and t_{centered}. These are obtained after centering all datasets by normalizing with the mean N_{OH} and $N_{\mathrm{H_2}}$. The uncentered t is given by $t = t_{\mathrm{centered}} + \log(\overline{N_{\mathrm{OH}}}) - m \times \log(\overline{N_{\mathrm{H_2}}})$, as $t = 8.04^{+2.77}_{-2.88}$.

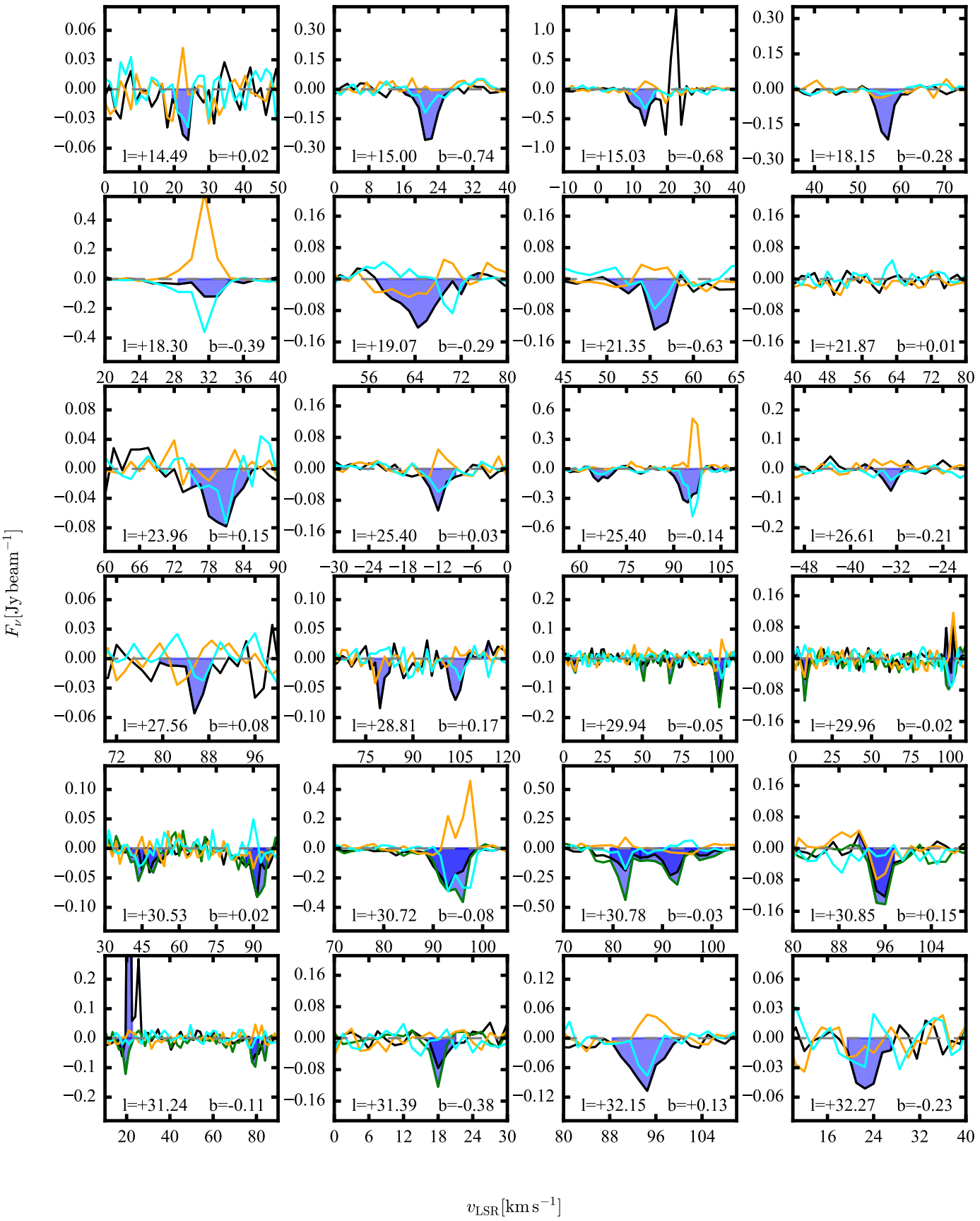

Fig. C.1. Spectra of OH ground state transitions, especially also of the satellite lines, along lines of sight that show a detection in 1665 MHz or 1667 MHz absorption. The spectra are extracted from data cubes that have been smoothed to 46″ resolution. The transitions at 1665 MHz (black), 1612 MHz (orange) and 1720 MHz (cyan) are shown for all sources. The 1667 MHz (green) transition is displayed if available. OH absorption detections in the main line transitions are shaded in blue.

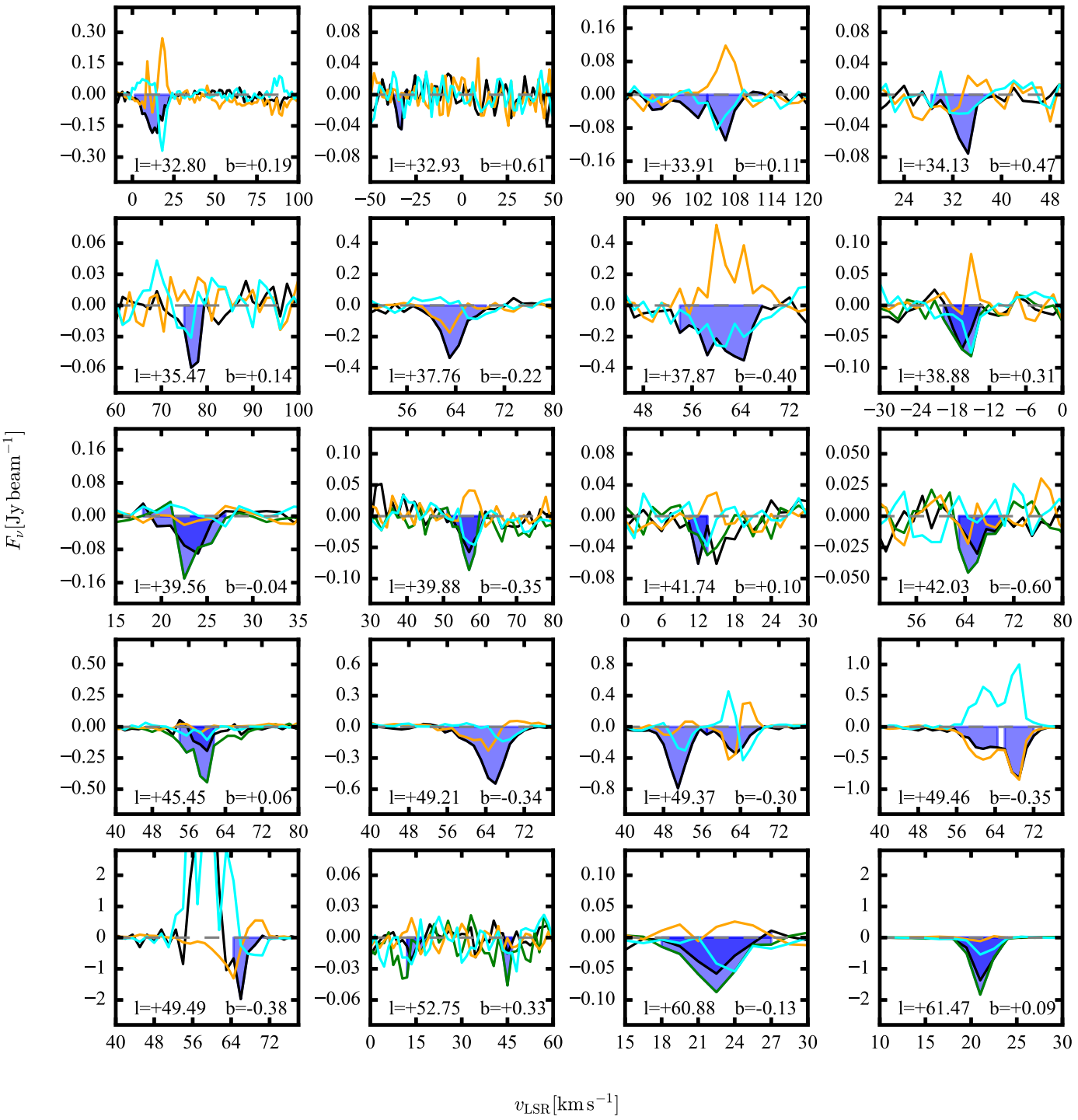

Fig. C.2. As Fig. C.1.

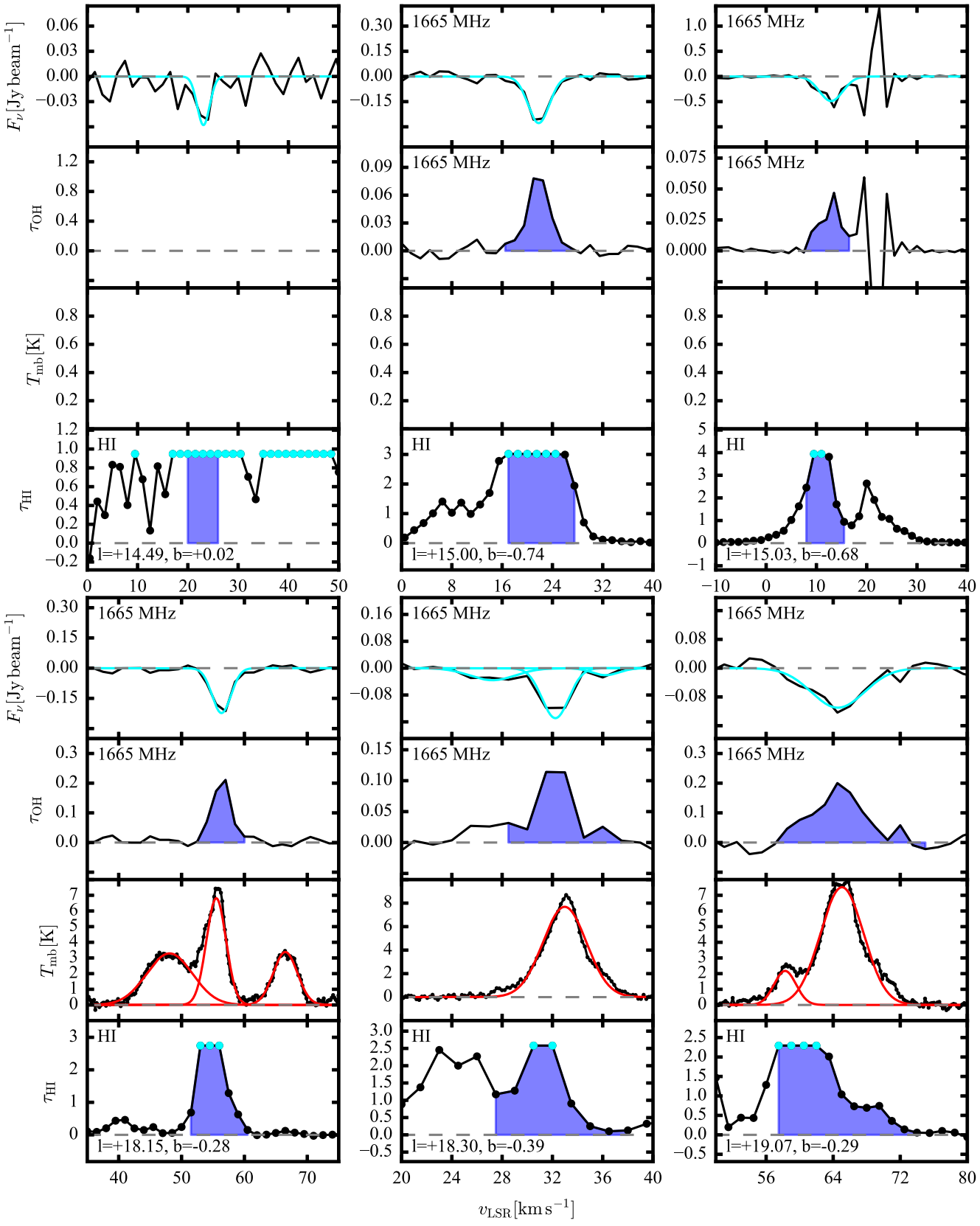

Fig. D.1. Analyzed 1665 and 1667 MHz OH absorption features. The topmost panel shows 1665 MHz (black) and 1667 MHz (green) absorption features. The second panel from the top shows the spectrum converted to optical depth for the 1665 MHz (black) and 1667 MHz (green) transition. The third panel from the top shows the ^{13}CO(1 − 0) emission in $T_{\rm mb}$. The line widths were determined by fitting Gaussian profiles to the 1665 MHz (cyan) and 1667 MHz (orange) absorption spectra, and the ^{13}CO(1 − 0) emission (red). The lowermost panel shows the H I absorption converted to H I optical depth. Measured bins are denoted by black dots, while we quote lower limits (cyan) for saturated bins. The 1667 MHz transition was observed only towards selected regions and is therefore shown only for a subset of lines-of-sight (see Sect. 2). The line-of-sight coordinates are given in degrees of Galactic coordinates. The blue shaded area in the lower three panels shows the line integrals. All data were smoothed to a spatial resolution of 46″.

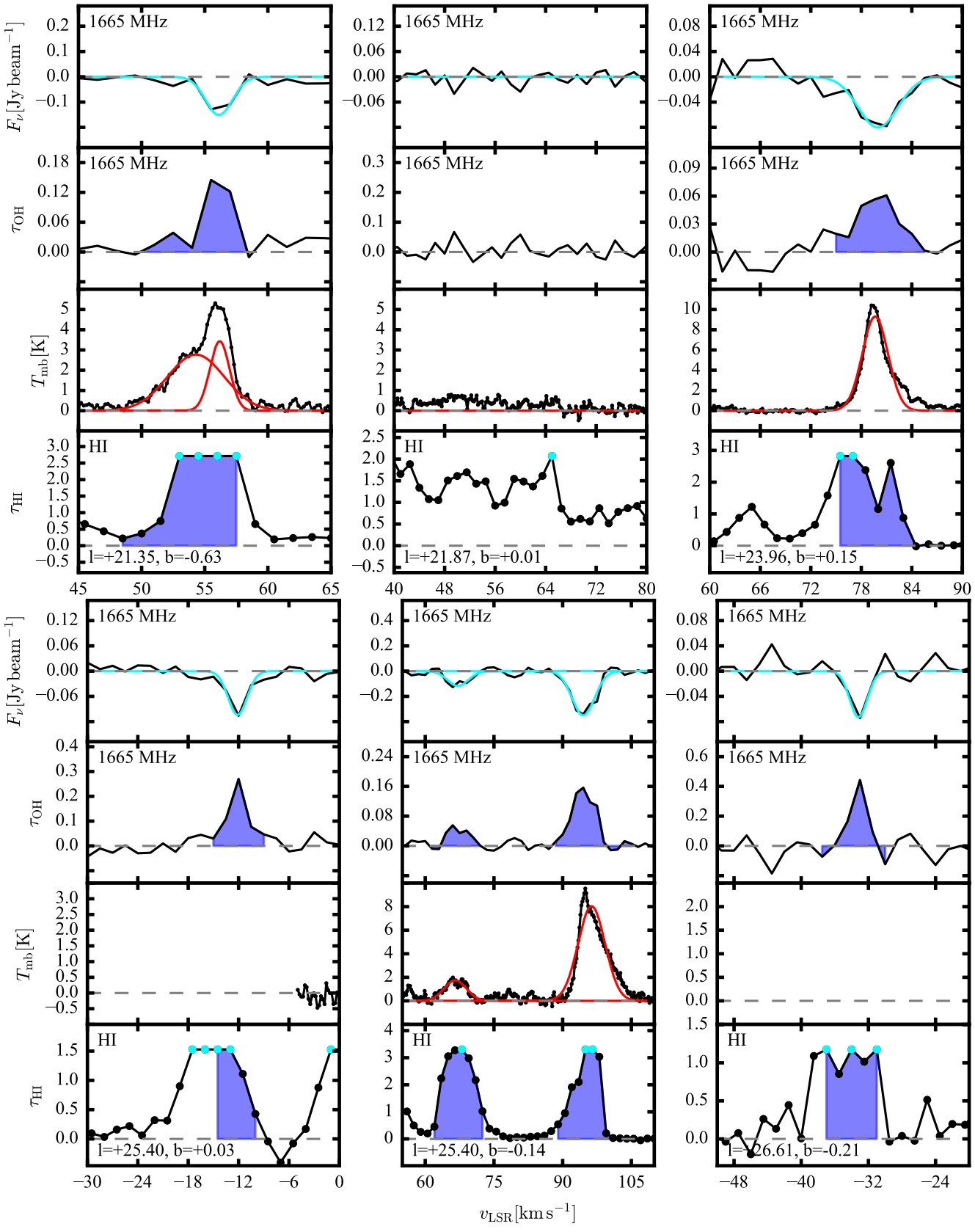

Fig. D.2. As Fig. D.1.

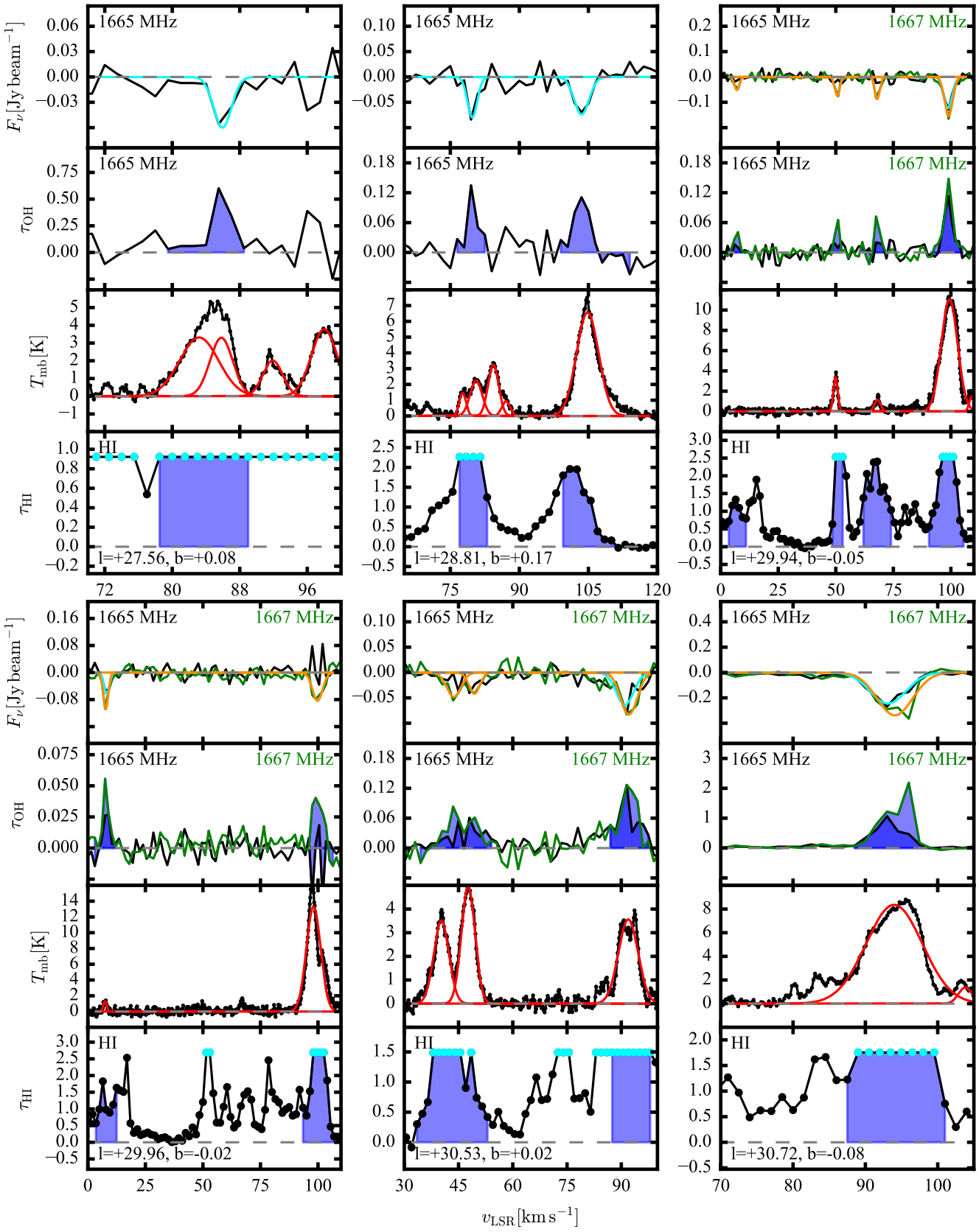

Fig. D.3. As Fig. D.1.

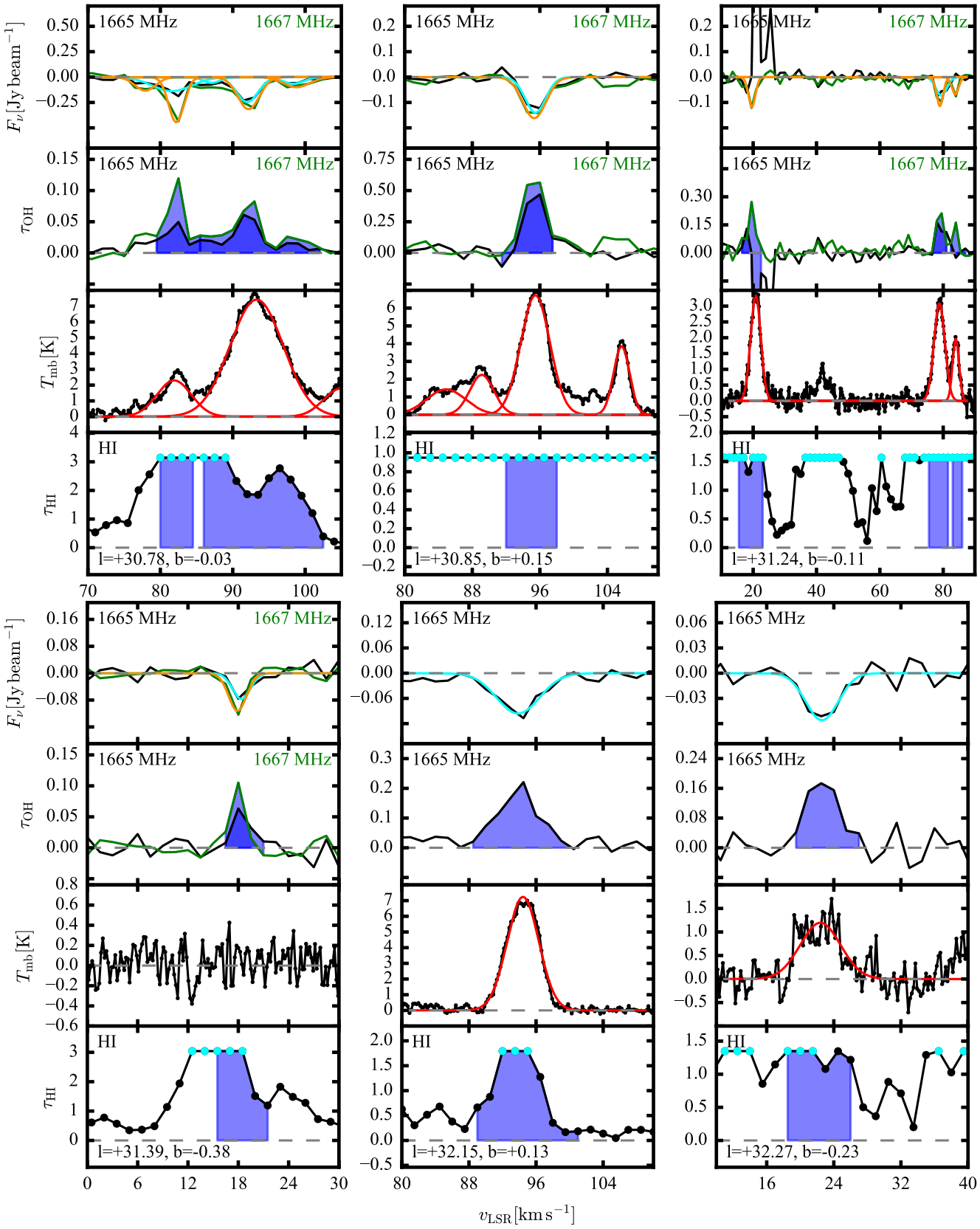

Fig. D.4. As Fig. D.1.

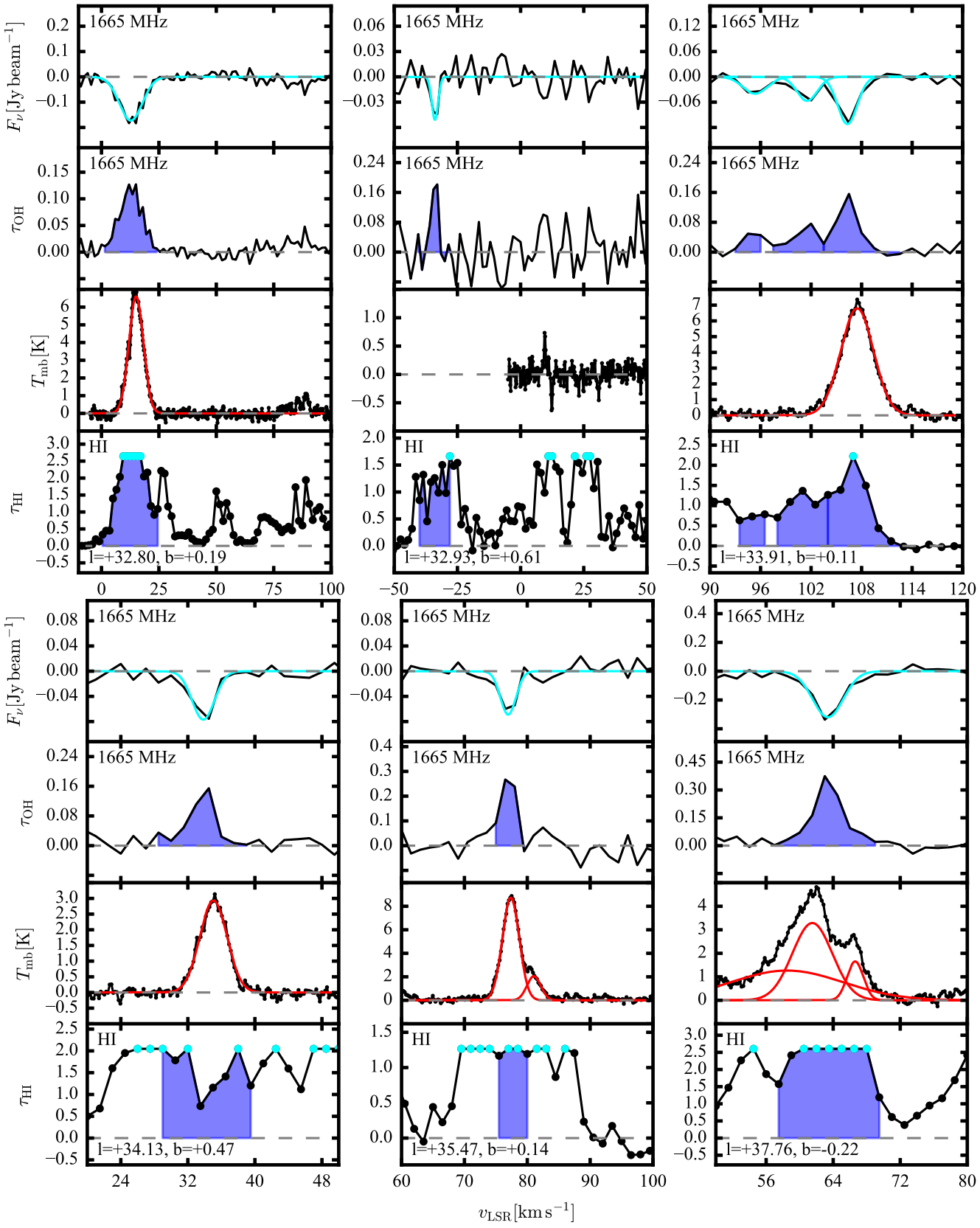

Fig. D.5. As Fig. D.1.

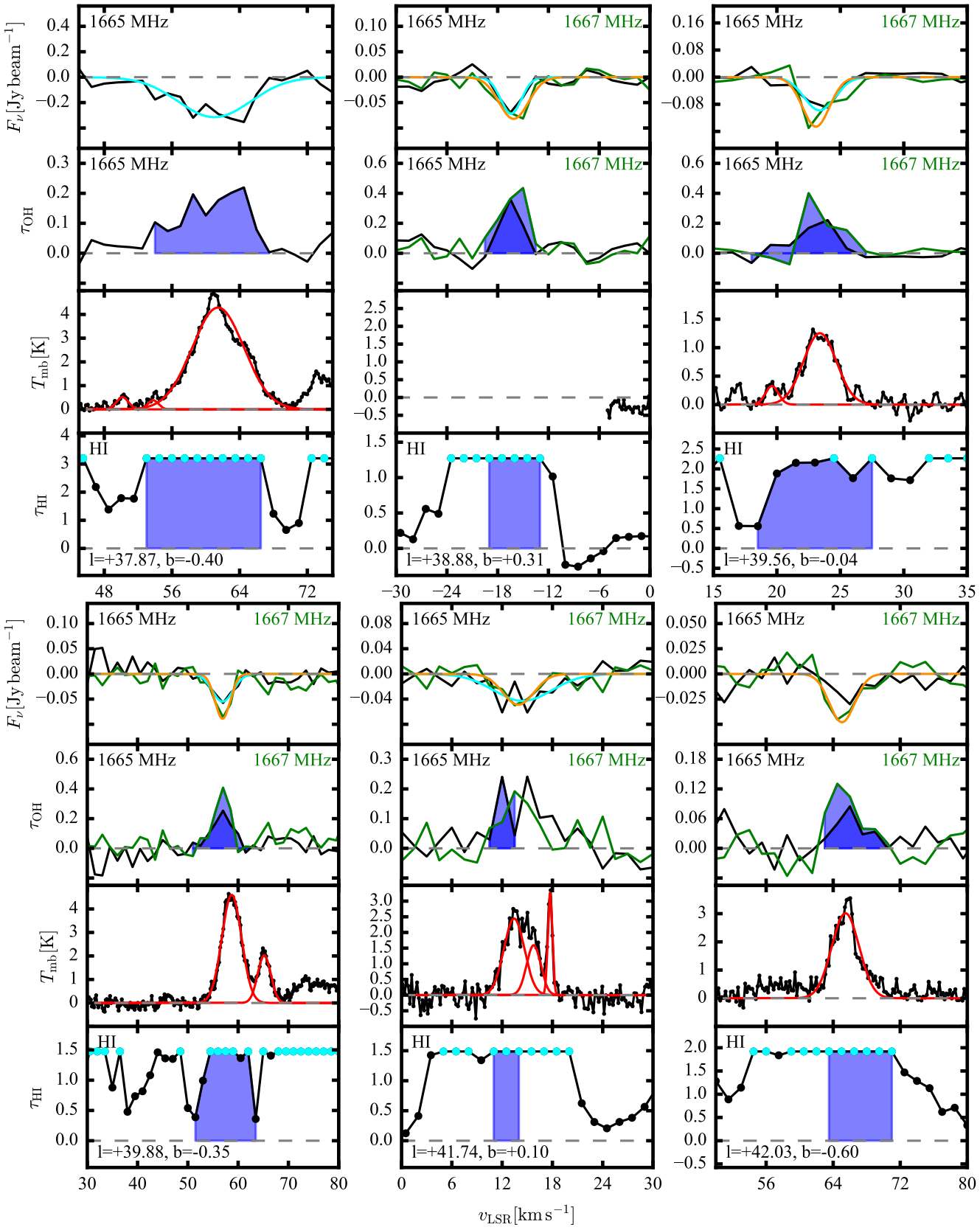

Fig. D.6. As Fig. D.1.

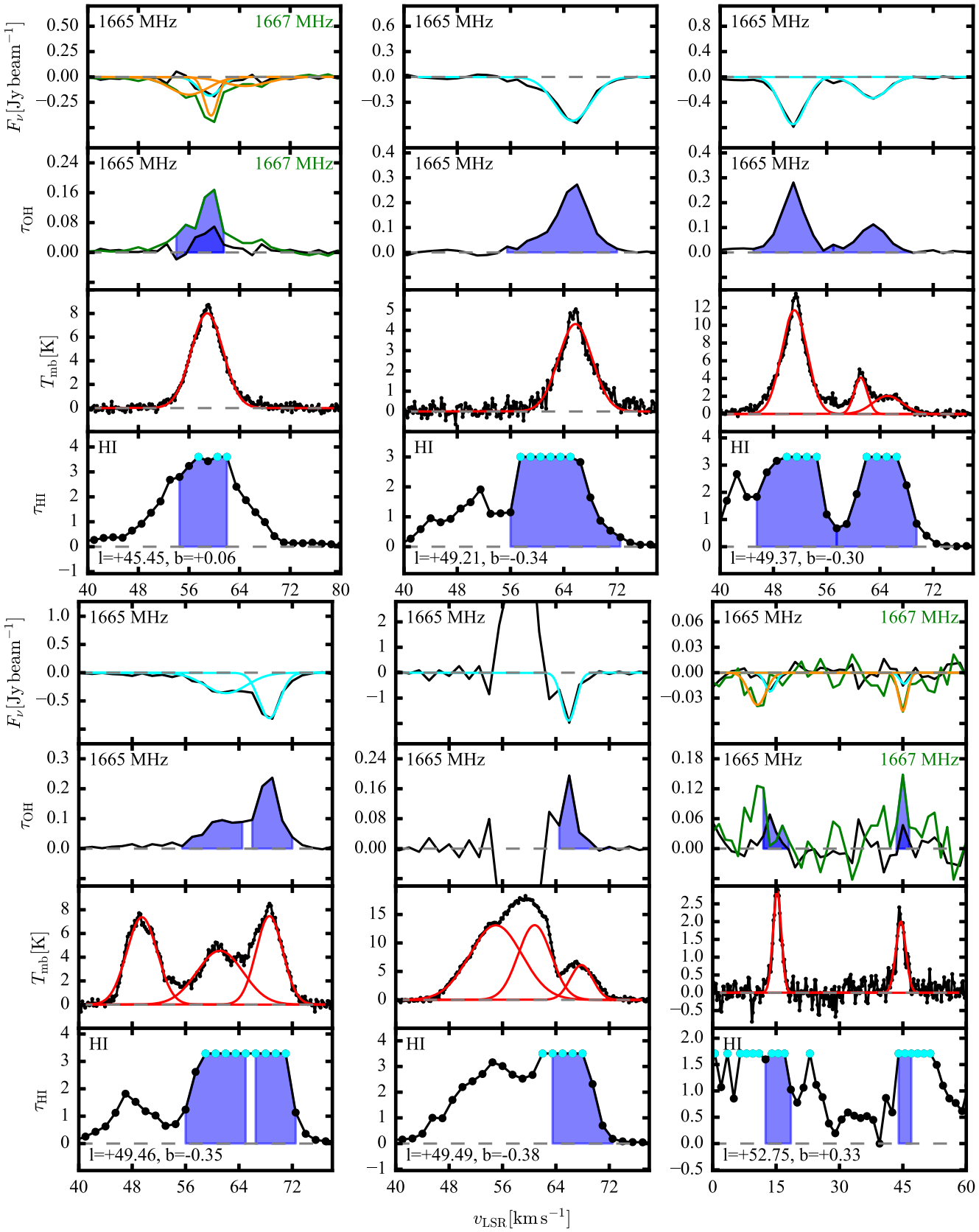

Fig. D.7. As Fig. D.1.

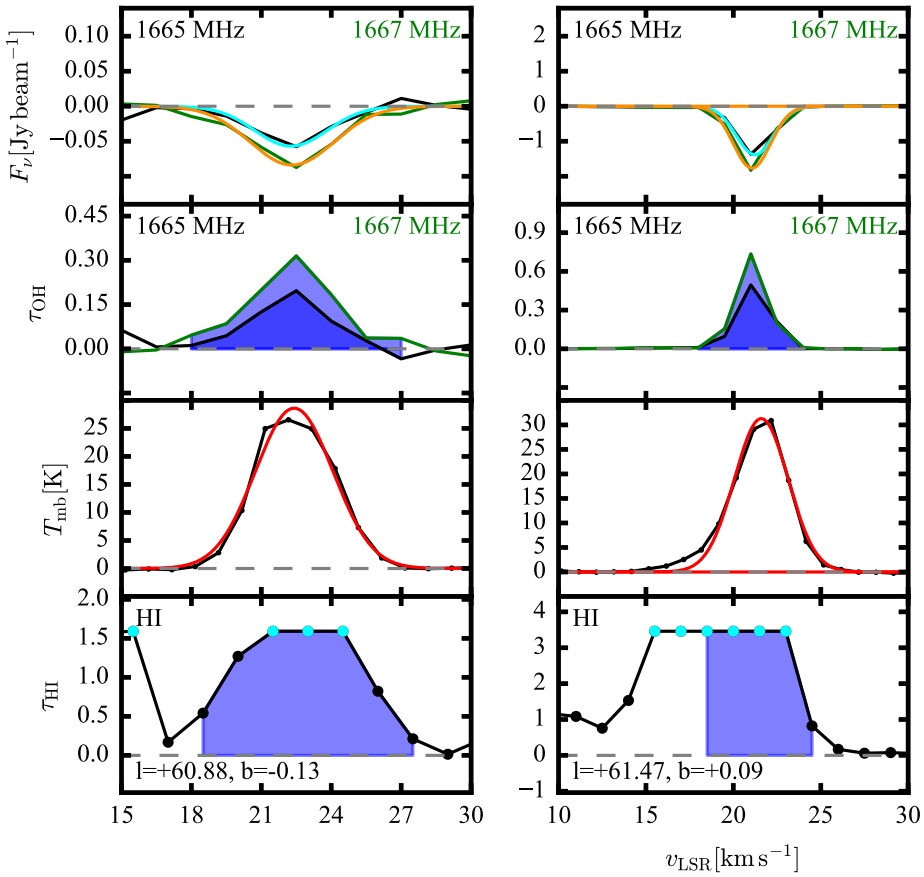

Fig. D.8. As Fig. D.1.

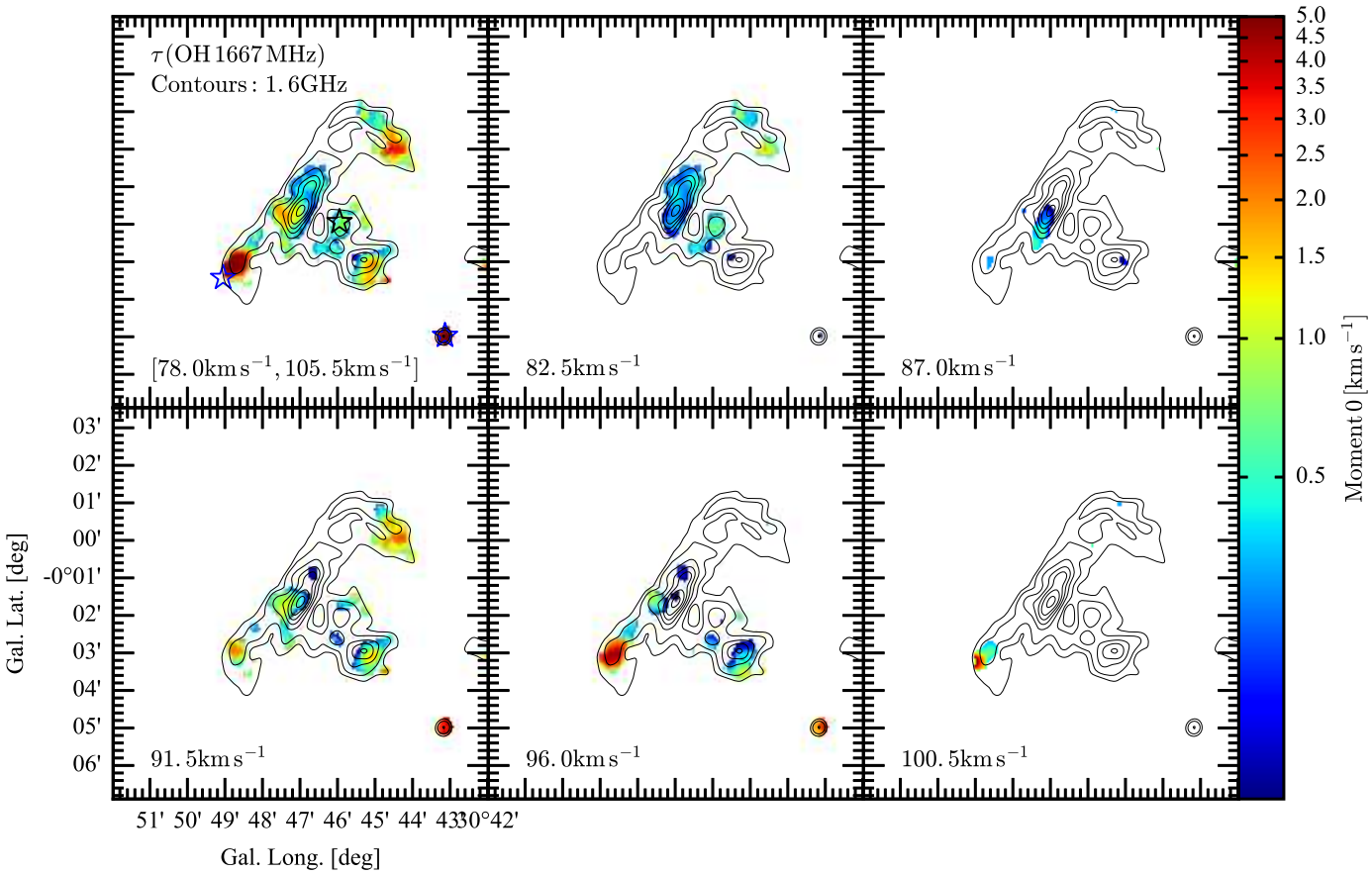

Fig. E.1. Integrated optical depth of the OH 1667 MHz line in the W43 star-forming region. In the top-left panel, τ is integrated over the same velocity range as in Fig. 10. The other panels show τ around the indicated velocities after integrating over three channels of 1.5 km s^{-1} width. For each pixel, only channels that are detected at a 3-σ level or higher contribute to the integrated τ-map. The optical depth map is overlayed with contours of the 18 cm continuum emission (black, in levels of 0.1, 0.2, 0.4, 0.6, 0.8, 1.0, 1.25, 1.5 and 1.75 Jy beam^{-1}). Symbols as in Fig. 10.